1  **Sonar Gas Flux Estimation by Bubble Insonification: Application to Methane Bubble Flux**
2  **from Seep Areas in the outer Laptev Sea**

3  Ira Leifer[1,], Denis Chernykh[2,3], Natalia Shakhova[3,4], and Igor Semiletov[2,3,4]

4  [1] Bubbleology Research International, Solvang, CA 93463

5  [2] Russian Academy of Science, Pacific Oceanological Institute, Vladivostok, Russia

6  [3] National Tomsk Research Polytechnic University, Tomsk, Russia

7  [4] University Alaska Fairbanks, International Arctic Research Center, Fairbanks, USA

8  **Abstract**

9  Sonar surveys provide an effective mechanism for mapping seabed methane flux emissions, with Arctic

10  submerged permafrost seepage having great potential to significantly affect climate. We created *in situ*

11  engineered bubble plumes from 40-m depth with fluxes spanning 0.019 to 1.1 L/s to derive the *in situ*

12  calibration curve ($Q(\sigma)$). These non-linear curves related flux ($Q$) to sonar return ($\sigma$) for a multibeam

13  echosounder (MBES) and a single beam echosounder (SBES) for a range of depths. Analysis

14  demonstrated significant multiple bubble acoustic scattering – precluding the use of a theoretical

15  approach to derive $Q(\sigma)$ from the product of the bubble $\sigma(r)$ and the bubble size distribution where $r$ is

16  bubble radius. The bubble plume $\sigma$ occurrence probability distribution function ($\Psi(\sigma)$) with respect to $Q$

17  found $\Psi(\sigma)$ for weak $\sigma$ well described by a power law that likely correlated with small bubble dispersion

18  and was strongly depth dependent. $\Psi(\sigma)$ for strong $\sigma$ largely was depth-independent, consistent with

19  bubble plume behavior where large bubbles in a plume remain in a focused core. $\Psi(\sigma)$ was bimodal for

20  all but the weakest plumes.

21  $Q(\sigma)$ was applied to sonar observations of natural arctic Laptev Sea seepage after accounting for

22  volumetric change by numerical bubble plume simulations. Simulations addressed different depths and

23  gases between calibration and seep plumes. Total mass fluxes ($Q_m$) were 5.56, 42.73, and 4.88 mmol/s for

24  MBES data with good to reasonable agreement (4-37%) between the SBES and MBES systems. The

25  seepage flux occurrence probability distribution function ($\Psi(Q)$) was bimodal, with weak $\Psi(Q)$ in each

26  seep area well described by a power law, suggesting primarily minor bubble plumes. Seepage mapped

27  spatial patterns suggested subsurface geologic control attributing methane fluxes to the current state of

28  subsea permafrost.

29  **Keywords:** Bubble, multibeam sonar, single beam, quantification, Arctic, methane, submerged

30  permafrost, field study, seep, engineered bubble plume

## 1. Introduction

### 1.1 Arctic Methane

On a century timescale, methane ($CH_4$) is the next most important anthropogenic greenhouse gas after carbon dioxide ($CO_2$) (Forster et al. 2007). However, on a decadal time scales comparable to its atmospheric lifetime, $CH_4$ is more important to the atmospheric radiative balance than $CO_2$ (IPCC, 2007; Fig 2.21). After nearly stabilizing, atmospheric $CH_4$ concentrations are increasing again, although the underlying reasons remain poorly understood (Nisbet et al., 2014). Despite likely increasing future natural emissions from global warming feedbacks (Rigby et al., 2008) and anthropogenic activities (Kirschke et al., 2013; Wunch et al., 2009). Many source estimates have large uncertainties with greater uncertainty in future trends, particularly for Arctic sources where global warming is the strongest (Graversen et al., 2008).

Arctic continental shelf sediment accumulates 5 times faster than other World's Oceans. Sedimentation for the Siberian Arctic shelf where the six Great Siberian Rivers outflow, has deposited organic carbon that approximately equals accumulations over the entire pelagic area of the World's Oceans. This leads to the thickest (to 20 km) and most extensive sedimentary basin in the world (Gramberg et al., 1983).

Terrestrial Arctic permafrost $CH_4$ provides important climate feedbacks (Friedlingstein et al., 2006; Lemke et al., 2007) as does sub-sea permafrost - submerged terrestrial permafrost (Shakhova and Semiletov, 2009). Subsea permafrost degradation drives seabed $CH_4$ bubble emissions. Assessing these emissions is challenging due to the vast extent of the East Siberian Arctic Shelf (ESAS) seep field (Shakhova et al., 2014; Stubbs, 2010), the world's most extensive seep field.

Sonar is the most common survey approach and has been used on concentrated seep areas covering ~1000 $m^2$ in the North Sea (Schneider von Deimling et al., 2007; Schneider von Deimling et al., 2010; Wilson et al., 2015), far more dispersed and weaker seepage in the Black Sea of ~2500 plume in an areas of ~20 $km^2$ (Greinert et al., 2010), and offshore Svalbard where a few hundred plumes were observed in an area of ~ 15 $km^2$ (Veloso et al., 2015). Sonar also can be used from remotely operated vehicles for the deep sea e.g., Muyakshin and Sauter (2010) for the Hakon-Mossby mud volcano (3 plumes).

Sonar also has mapped significantly larger and stronger seepage in the Coal Oil Point (COP) marine hydrocarbon seep field, offshore California. The COP seep field covers ~3 $km^2$ of active seabed in an 18 $km^2$ area releasing $10^5$ $m^3$ $CH_4$ per day (Hornafius et al., 1999), likely comprised of many tens of thousands of plumes. A single survey requires two days (Leifer et al., 2010).

ESAS seepage is on a dramatically larger scale with ~30,000 plumes manually identified in just two transects (Shakhova et al., 2014; Stubbs, 2010). Seepage densities to ~3000 seep bubble plumes per $km^2$ were found transecting a single hotspot. Based on the hotspot size (18,400 $km^2$), an order of magnitude estimate suggests 60 million seep plumes for the hotspot alone. Two sonar survey transits of the ESAS required a month.

**1.2 Study motivation**

Given the ESAS seepage extent there is a critical need for new approaches to effectively, rapidly, and quantitatively survey seepage areas. Video is inadequate to survey extensive or widely dispersed seepage, a task for which sonar (active acoustics) excels. This study demonstrates an improved approach to quantify seabed seepage using *in situ calibrated* sonar-derived bubble fluxes. Bubble plumes were observed in the ESAS and offshore California. In combination, the *in situ* studies covered a broad range of flows and included fine depth resolution of near source (growth) plume processes (California) and coarser resolution of plume processes to tens of meters where the plume is self-similar (ESAS).

Both multiple beam echosounder (MBES) and single beam echosounder (SBES) data were collected in the ESAS, just MBES in California of rising engineered bubble plumes. These data were collected both as a depth dependent calibration and to investigate the effect of multiple acoustic scattering in bubble plumes.

The calibration was applied to quantify *in situ* sonar observations of three natural seepage areas in the ESAS. Because the calibration bubble plumes and seep bubble plumes were different gases and from different source depths, bubble dissolution rates are different – i.e., for the same seabed mean volume flux, the depth-window-averaged volume fluxes are different. We demonstrate a first correction attempt based on a numerical bubble-plume model between the calibration and natural seepage bubble flows.

**1.2 The East Siberian Arctic Shelf**

The Siberian Arctic Shelf contains vast $CH_4$ deposits as subsea permafrost, $CH_4$ hydrates, and natural gas reservoirs (Gautier et al., 2009; Gramberg et al., 1983; Romanovskii et al., 2005; Serreze et al., 2009; Shakhova et al., 2010a; Shakhova et al., 2010b; Shakhova and Semiletov, 2009). Reservoir estimates are ~10,000 gigatonnes Gt (1 Gt=$10^{15}$g) of $CH_4$ hydrates (Dickens, 2003). Remobilization of even a small fraction of this $CH_4$ could trigger abrupt climate warming - Archer and Buffett (2005) estimated atmospheric release of just 0.5% of the Arctic shelf hydrate $CH_4$ could cause abrupt climate change.

The ESAS is the world's largest and shallowest shelf (covering 2.1x$10^6$ $km^2$) containing the largest area of submerged permafrost by far (Shakhova et al., 2010a; Shakhova et al., 2010b). The ESAS is a seaward

extension of the Siberian tundra that was flooded during the Holocene transgression, 7-15 kyr ago (Romanovskii et al., 2005). The ESAS comprises ~25% of the Arctic continental shelf and contains over 80% of global subsea permafrost and shallow hydrate deposits, estimated at ~1400 Gt carbon (Shakhova et al., 2010a). This reservoir includes hydrate deposits of $\sim$540 Gt of $CH_4$ with an additional 2/3 ($\sim$360 Gt) trapped below as free gas (Soloviev et al., 1987).

*Permafrost Degradation*

ESAS subsea permafrost degradation allows the release of sequestered $CH_4$ to the shallow ocean and atmosphere and is changing in response to glacial/interglacial Arctic warming (~7°C) and warming from the overlying seawater (~10°C) since inundation in the early Holocene, with additional ESAS seawater warming in recent decades (Biastoch et al., 2011; Semiletov et al., 2013; Semiletov et al., 2012; Shakhova et al., 2014).

Onshore and offshore Arctic permafrost can thaw from the top downward, with the active layer expanding, downward creating taliks (bodies of thawed permafrost). They also degrade bottom up from geothermal heat flux, thawing frozen sediments from below (Osterkamp, 2010; Shakhova and Semiletov, 2009). The latter only has a significant effect for submerged offshore permafrost (Romanovskii et al., 2005). Recent observations of offshore permafrost (Shakhova et al., 2014) show the ESAS permafrost lid is perforated, with all year round $CH_4$ emissions to the atmosphere from the sedimentary reservoir (Shakhova et al., 2010a; Shakhova et al., 2015). This migration feeds a vast marine seep field entirely in shallow waters where emissions contribute directly to the atmospheric budget (Shakhova et al., 2014).

There are important geologic controls on the subsea permafrost's thermal state. On millennia time scales, increasing temperatures of the overlying bottom seawater affect subsea permafrost by heat transfer and salinization (Shakhova et al., 2014; Shakhova et al., 2015; Soloviev et al., 1987). Geologic control also arises from heat transport by large Siberian rivers which drives bottom water warming and is proposed to control the distribution of open taliks in coastal ESAS waters (Shakhova et al., 2014). Global warming enhances riverine heat from terrestrial including, ecosystem responses, degradation of terrestrial permafrost, and increased river runoff. Warm riverine runoff drives a downward heat flux to shelf sediments and subsea permafrost (Shakhova and Semiletov, 2007; Shakhova et al., 2014).

Heat flow in rift zones also provides geologic control (Drachev et al., 2003; Nicolsky et al., 2012). High heat flow areas include relic–thaw lakes and river-valleys that were submerged during the Holocene inundation. These still drive modern permafrost degradation (Nicolsky and Shakhova, 2010; Nicolsky et al., 2012; Shakhova and Semiletov, 2009).

4

Subsea permafrost degradation is greatest in the outer shelf waters (deeper than 50 m) where submergence occurred first, such as the outer Laptev Sea where models predict mostly degraded permafrost (Bauch et al., 2001). Riverine input to the Laptev Sea also supports the formation and growth of subsea thaw lakes and taliks, which are effective gas migration pathways to the seabed (Hölemann et al., 2011; Nicolsky and Shakhova, 2010; Shakhova and Semiletov, 2007; Shakhova et al., 2014).

Active seafloor spreading in the Laptev Sea, which is converting into continental rifting, leads to strong geologic heat flow (85-117 m W m$^{-2}$). The outer Laptev Sea is one of the few places where active oceanic spreading approaches a continental margin (Drachev et al., 2003) and correlates with the "hot" area crossed by the Ust' Lensky Rift and Khatanga-Lomonosov Fracture (Drachev et al., 2003; Nicolsky et al., 2012). Evidence of rifting is provided by hydrothermal fauna remnants documented around grabens (dropped blocks between faults) in the up-slope area that typically occur along oceanic divergent axes (Drachev et al., 2003). Grabens in the ESAS often are linear structures that correlate spatially with paleo-river valleys.

## 1.3. Marine seepage fate and bubble processes

Marine seepage is a global phenomena where $CH_4$ and other trace gases escape the seabed as bubbles that rise towards the sea surface (Judd and Hovland, 2007). These bubbles dissolve and deposit $CH_4$ in the water column, transporting their remaining contents to the sea surface – if they reach it (Leifer and Patro, 2002). The fate of these bubbles and their gas depends strongly on depth and size (Leifer and Patro, 2002), and flow strength – plume synergies that includes the upwelling flow (Leifer et al., 2009) and bubble surface properties, like contamination (Leifer and Patro, 2002).

The fate of dissolved seep $CH_4$ depends most strongly on its deposition depth (Leifer and Patro, 2002) with $CH_4$ below the Winter Wave Mixed Layer (WWML) largely oxidized microbially (Rehder et al., 1999). In the shallow Coal Oil Point (COP) seep field, most of the $CH_4$ reaches the atmosphere directly (Clark et al., 2005) from mixing in the near field (Clark et al., 2000) and in the far (down-current) field when winds strengthen as typical occurs diurnally for coastal California. The same is true for the shallow ESAS where virtually all the seabed $CH_4$ (dissolved and gaseous) is emitted in the WWML and escapes to the atmosphere directly or from frequent storms (Shakhova et al., 2014). Even for deepsea seepage (to ~1 km), field studies show seep bubble-plume $CH_4$ transport to the upper water-column and atmosphere (MacDonald, 2011; Solomon et al., 2009) from plume processes and hydrate skin effects (Rehder et al., 2009; Warzinski et al., 2014).

Bubble size is important with most seep bubbles in a narrow range. Based on a review of 39 bubble-plume size distributions (the most comprehensive published dataset to date), Leifer (2010) found that the

vast majority of reported seep bubble plumes could be classified in two categories, termed major and minor. Minor are the most common - see also studies reviewed in Leifer (2010). Bubble-plume size distributions ($\Phi(r_e)$) for minor bubble plumes are well described as Gaussian and largely comprised of bubbles in a narrow size range, $1000 < r_e < 4000$ μm, where $r_e$ is the equivalent spherical radius. Major bubble plumes generally escape from higher flow vents with a power law size distribution (Leifer and Culling, 2010). Most major bubble plumes are small (to $r_e < 100$ μm); however, plume volume is primarily in the largest bubbles, to $r_e \sim 1$ cm (Leifer et al., 2015b).

**1.3 Sonar Seep bubble observations**

Seep $\Phi(r_e)$ have been measured by video (Leifer, 2010; Römer et al., 2012; Sahling et al., 2009; Sauter et al., 2006) and passive acoustics. Passive acoustic $\Phi(r_e)$ measurement only has been demonstrated for low-flow bubble plumes where the individual bubble acoustic signatures can be identified (Leifer and Tang, 2006; Maksimov et al., 2016).

Sonar interpretation is highly challenging, even for qualitative assessment of relative emission strength. For single beam echosounders (SBES), there is geometric uncertainty (Leifer et al., 2010) – the plume's angular location is unknown; a problem resolved by multibeam echosounders (MBES). Additionally, sonar (SBES or MBES) loses fidelity from multiple plumes in close proximity (Schneider von Deimling et al., 2011; Wilson et al., 2015) where the sonar returns along multiple pathways, creating ghosts, shadow noise, off-beam returns, scattering loss, and other artifacts (Wilson et al., 2015). Note, if bubble spatial densities are sufficiently high for artifacts to occur between plumes, then bubbles inside the plume will produce artifacts inside the plumes. The vessel acoustic environment can be noisy and signal loss from scattering also can occur from suspended sediment and biota, often in layers.

There are many challenges to quantitative derivation of bubble emission flux from sonar return, which at its basis relates to the interaction of sound with a bubble. For a single spherical bubble the relationship has long been known, with resonance given by the Minnaert (1933) equation:

$$f_o = \frac{1}{2\pi r}\left(\frac{3\gamma P}{\rho}\right)^{1/2} \tag{1}$$

where $f_o$ is the resonance (or Minnaert) frequency, $\gamma$ is the resonance (or Minnaert) frequency, $P$ is internal bubble gas pressure, and $\rho$ is pressure. This is the frequency a bubble emits at formation. For non-spherical bubbles ($r_e > 150$ μm) there is an eccentricity correction based on the bubble-axis-wave front angle. Bubble eccentricities vary from 1.0 for spherical bubbles to 2 or greater for $r_e > 3500$ μm

6

1 (Clift et al., 1978). For a single spherical bubble, the back-scattering cross section (σ) near $f_o$ is (Weber et

2 al., 2010):

3
$$\sigma = \frac{r_e^2}{\left[\left(\frac{f_o}{f}\right)^2 - 1\right]^2 + \delta^2}$$
(2)

4 where $f$ is frequency and δ is the damping term, approximated as $\delta \sim 0.03 f^{0.3}$ with $f$ in kHz. For bubbles

5 larger than resonance, σ varies within 5 or so db, for bubbles smaller than resonance it decreases

6 precipitously – 35 db for a factor 2 decrease in $r_e$ (Weber et al., 2014). Integrating over the bubble

7 emission size distribution ($\Phi(r_e)$), which is the number of bubbles in a $r_e$ bin, passing through the

8 measurement plane, combined with the bubble vertical velocity ($V_Z(r_e)$), which is a function of $r_e$ over the

9 measurement volume yields the total plume cross-section if bubbles are acoustically non-interfering (no

10 multiple scattering) and the bubble-sonar interaction is isotropic – i.e., $\sigma_B$ is independent of angle despite

11 bubble eccentricity.

12 However, bubbles are often in close proximity in seep bubble plumes – clustered, which allows multiple

13 scattering between bubbles that decreases σ significantly (Weber, 2008). Acoustic modeling of bubble

14 clusters is complicated, even for small spherical bubbles – e.g., see Weber (2008). Specifically σ depends

15 on $\Phi(r_e, x, y, z)$ in the plume, which is asymmetric from currents and evolves as the bubble plumes rises.

16 Acoustic propagation across a plume also varies with azimuthal angle because bubbles are compressible

17 and from bubble eccentricity. Whereas artifacts, like ghosting between plumes (not side lobe return), can

18 be spatially segregated, this is not feasible for such artifacts inside the plume. Where the bubbles are

19 within a few centimeters (~10-20 $r_e$), such as bubbles in the wake of a larger bubble (Tsuchiya et al.,

20 1996) and near the seabed, acoustic coupling leads to frequency shifts (Leifer and Tang, 2006) that

21 decrease σ.

## 2. Methodology

### 2.1. Field Study areas

24 This study reports on the use of *in situ* engineered plumes for calibration of σ to derive quantitative flux

25 rates using a MBES which was deployed in the Coal Oil Point (COP) seep field, offshore California in the

26 northern Santa Barbara Channel, in the Kara Sea of the ESAS. We present the small fraction of collected

27 Kara Sea and ESAS data that were cleared for publication.
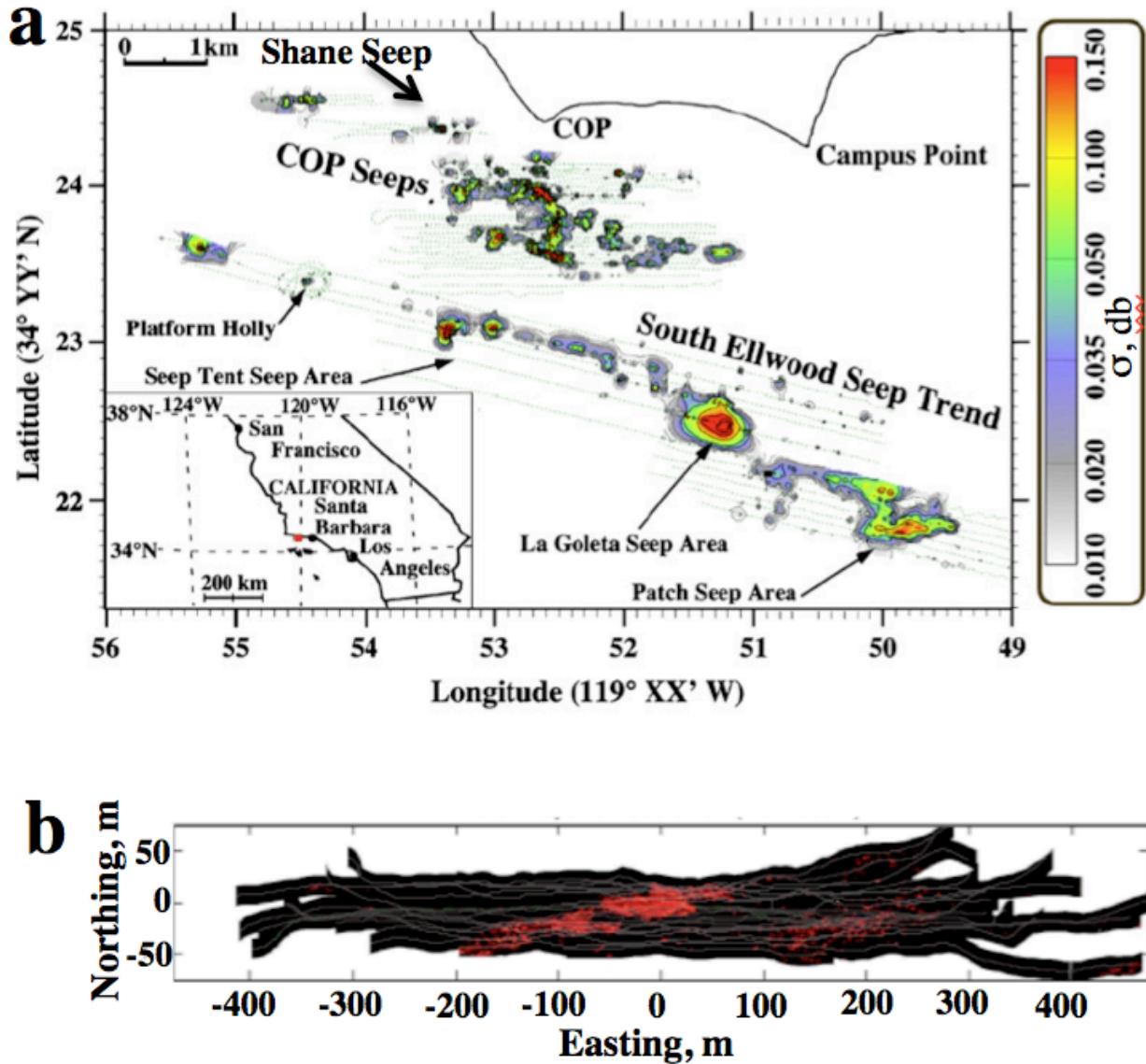
**Figure 1. a.** Coal Oil Point (COP) seep field map, showing the Shane Seep area of the scoping study. Sonar data from 2005. Adapted from Leifer et al. (2010). **b.** Shane Seep multibeam sonar survey map of seep detection (2-m depth window at a seabed-following height of 4 m). MBES data collected in 2009.

**2.1.1. Coal Oil Point seep field**

A precursor study was conducted in the COP seep field (**Fig. 1**) prior to the Arctic field experiment to demonstrate 4D seep monitoring by a scanning MBES (**Supp. Fig. S1**). The rotator-lander was deployed ~15 m from the center of Shane Seep, which covers an area of ~$10^4$ m$^2$ in ~20-m water depth and comprises on the order of 1000 individual vents or bubble plumes (**Fig. 1B**). The lander included a MBES (DeltaT, Imagenex, Vancouver, Canada) and compass (Ocean Server, MA) on an underwater rotator (Sidus Solutions, CA) with azimuthal rotation of up to 270° angle range. The sonar produced a 260 kHz,

1    vertically-oriented 128-beam fan spanning 120°, tilted upwards to reduce seabed backscatter. Two *in situ*

2    calibration air bubble flows were deployed ~8 m from the lander at azimuthal angles beyond the active

3    seepage area and were traversed during each sonar rotation cycle. Two rotameters measured regulated

4    airflows from an onboard compressor to these two bubble plumes.
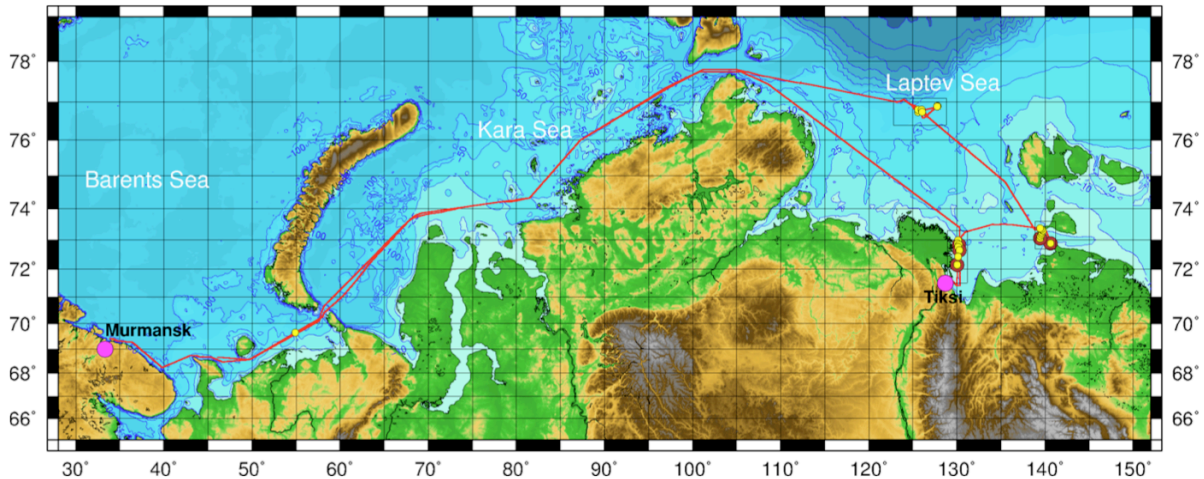


6    **Figure 2.** Map for the R/V *Victor Buynitsky* cruise, 2012.
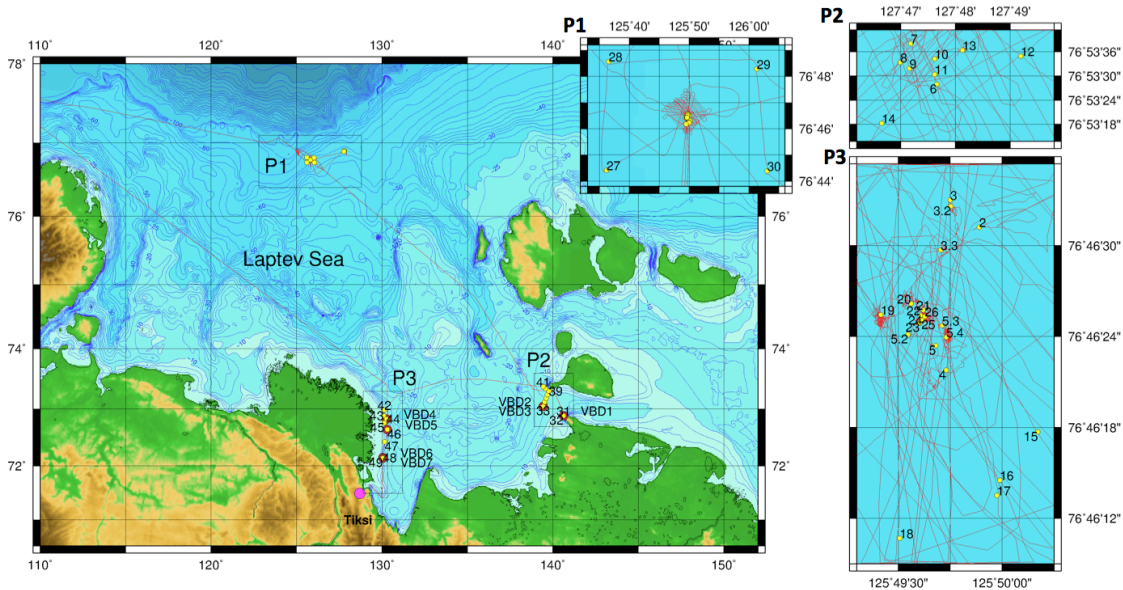


8    **Figure 3**. Locations of oceanographic stations for the RV *Victor Buynitsky* cruise, 2012, marked by

9    yellow circles. Polygons of major focus areas are marked as P1 (northern Laptev Sea), P2 (east Lena

10    Delta) and P3 (Dmitry Laptev Strait), shown in insets. Ship tracks accompanied by CTD measurements

11    (and geophysical survey) performed in the P1 are shown as red lines.

9

### 2.1.2 Arctic Field Campaign

Field data were obtained during an expedition onboard the research vessel R/V *Victor Buynitsky* from 2 Sept. to 3 Oct. 2012 (**Figs. 2 and 3**). The *Victor Buynitsky* sailed from Murmansk to the Laptev Sea and the adjacent portion of the ESAS. The expedition's overarching goal was to improve understanding of the current scale of ESAS $CH_4$ emissions in order to develop a conceptual model of $CH_4$ propagation from the seabed to the atmosphere, including assessing source strengths and their dynamics.

The calibration experiments were conducted in a region of no natural seepage and almost flat seafloor in the Kara Sea (**Fig. 3**) to reduce or eliminate off-beam acoustic seabed scattering. Water depths were 45-m and weather was favorable: calm sea with wind speed 1-3 m s$^{-1}$ and wave height of 0.2-0.5 m with no significant waves (0 to 1 ball). Column profile temperature and salinity data were measured by a conductivity temperature depth (SBE19+, Seabird, USA). Weather for the seep sonar survey was typical (3-4 storm events with wind speed >10 m s$^{-1}$).

The vessel was anchored during the engineered bubble plume experiments. Engineered bubble plumes were made from nitrogen supplied by a pressure tank on the vessel foredeck. A 70-m long, 12-mm diameter, 6-mm wall thickness, air supply tubing was attached by a Kevlar rope to a heavy metal weight (~30 kg) that ballasted against buoyancy of air in the tubing and drag from currents. The supply tube was deployed to 40-m depth in water of ~45-m depth (**Supp. Fig. S3**) and the rising bubble plume was observed with MBES and SBES. The sonars were located near each other so that their beam coverage overlapped with the center beam focused on the end of the bubble stream. Bubbles were produced from a 4-mm diameter copper nozzle attached at the end of the air supply tube.

Gas flow was controlled using standard flow meters, one port of which was connected to a PVC tube and another was connected to a 2-way valve, the second port of which was connected to the gas tank through the gas manifold. The manifold consisted of a high-pressure sensor of the tank pressure and a low-pressure sensor for the out-coming pressure (5.5 bar). We used temperature-compensated differential pressure sensors with a manufacturer-specified range of ±1 psi (equivalent to ±70 cm of water). The sensor has manufacturer-specified accuracy and stability of ±0.5% FSD (full scale deflection over the operating pressure range of the sensor over 1 yr, between 0 and 50°C) and repeatability errors of ±0.25% FSD. For the study, the gas flow was varied from 0.5 to 150 L min$^{-1}$ at 5.5 bar (equals the bubble outlet hydrostatic pressure). For each experiment, the gas flow was allowed to stabilize and then sonar data were recorded for ~10 minutes.

The same MBES was used in the ESAS and COP seep field. The SBES was a SIMRAD EK15 SW 1.0.0 echosounder (www.simrad.com) at 200 kHz, with a 1 ms pulse duration at 10 Hz, 26° beam width, and

10

1    built-in calibration system. Sonar data including seep bubble plumes were recorded at an average survey

2    speed of 4-6 knots. Sonar backscatter was calibrated using acoustic targets (SIMRAD, Denmark). Initial

3    data visualization and processing used EchoView and Sonar5 software (SIMRAD), for the EK15.

4    Bubbles have high density-contrast with water and thus are strong sonar targets that can be distinguished

5    easily from the background (**Fig. 4b**). For the engineered bubble plume experiments, the wave-mixed

6    layer (WML) extended to ~35 m depth with upper water warmer by ~3.5°C than deeper water (**Fig. 4a**).

7    Sonar data analysis and visualization was performed with custom MatLab routines (Mathworks, MA) that

8    first geo-rectified each ping and then assembled the data for each experimental run into a 3-dimensional

9    array of depth ($z$) transverse distance ($x$) and along track distance ($y$) or time ($t$) if stationary.
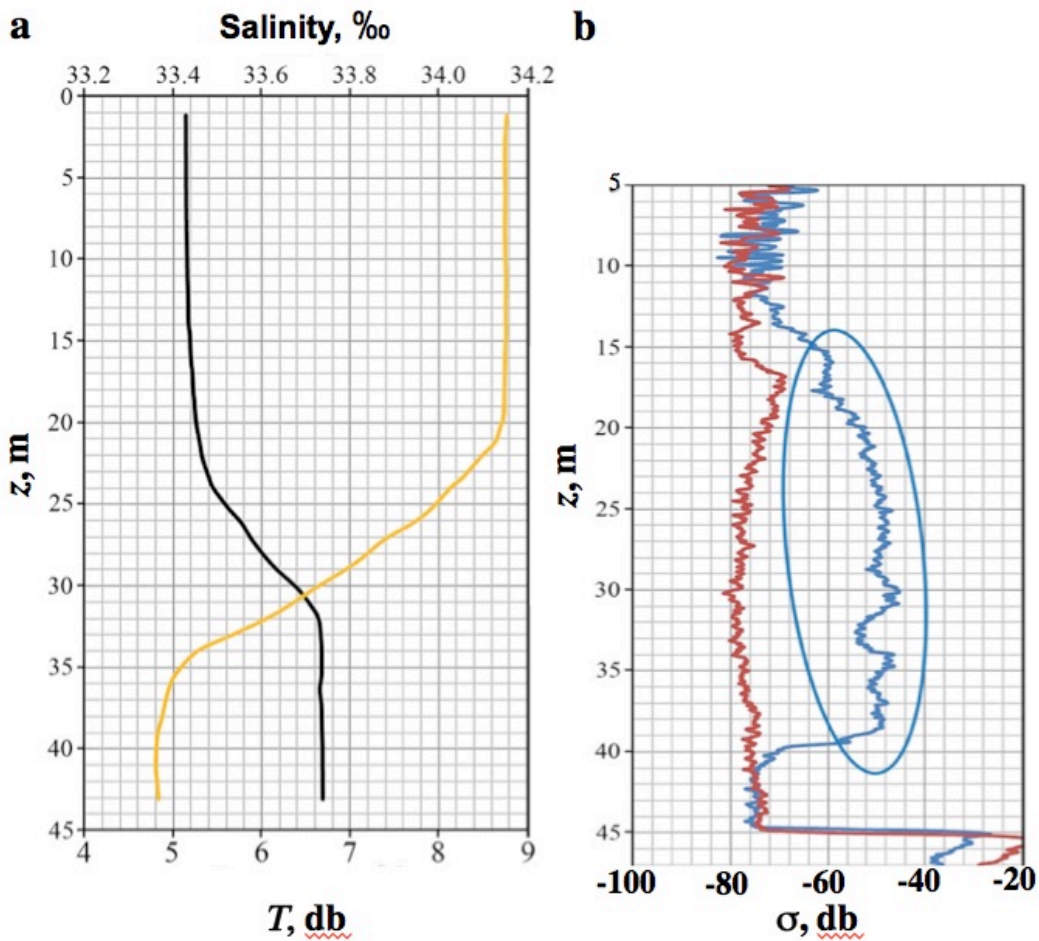
10



11    **Figure 4. a.** Salinity and temperature ($T$) with respect to depth ($z$) during engineered bubble plume

12    experiments. **b.** Single beam echosounder sonar return integrated across the plume ($\sigma$) with $z$ for no

13    bubble plume (red) and a bubble plume (blue), bubble plume $\sigma$ circled.

11

## 2. 2 Seep and engineered bubble plume modeling

A numerical bubble propagation model was used to explore the relative dissolution rates for seep versus calibration bubble plumes and to calculate a volumetric correction factor that accounted for the difference. The bubble model is described elsewhere (Leifer et al., 2006; Leifer and Patro, 2002; Leifer et al., 2015b; Rehder et al., 2009). The model solves the coupled differential equations describing bubble molar content (Eqn. 3), size (Eqn. 4), pressure, and rise for each bubble size class in a bubble plume. These equations describe how sonar observations of bubble volume (size) relate to bubble mass (molar content).

Bubble dissolution or gas flux ($F_i$) for each gas species $i$ is the change in bubble molar content ($n_i$) driven by the concentration difference ($\Delta C_i$ ) between the bubble and the surrounding water,

$$F_i = \frac{\partial n_i}{\partial t} = k_{Bi} A(\Delta C_i) = k_{Bi} A(C_i - H_i P_i) \tag{3}$$

where $k_B$ is the individual bubble gas transfer rate and depends on the gas diffusivity and $r_e$, $A$ is the bubble surface area, $H$ is the Henry's Law equilibrium, and $P$ is the bubble partial pressure. Seep gases, like methane largely outflow (positive $F$) while air gases inflow (negative $F$)

$F_i$ depends on depth and $r_e$ through $k_B$ and also $A$ (Leifer and Patro, 2002). Deeper bubbles of the same $r_e$ contain greater mass, allowing longer survival and rise. Seep bubbles are seldom isolated (Leifer, 2010), thus, plume processes are important, including the upwelling flow which depends on the total plume volume flux (Leifer et al., 2009; Leifer et al., 2006). Another plume process is enhanced aqueous concentrations relative to the surrounding water, which enhances bubble survival (Leifer et al., 2006).

$$\frac{\partial r_e}{\partial t} = \left\{ \mathbf{R}T \frac{\partial n}{\partial t} - \frac{4\pi r_e^3}{3} \rho_w g \frac{\partial z}{\partial t} \right\} \left\{ 4\pi r^2 \left( P_A - \rho_W g z + \frac{2\alpha}{r_e} \right) - \frac{4\pi r^3}{3} \frac{2\alpha}{r_e^2} \right\}^{-1} \tag{4}$$

were $\mathbf{R}$ is the universal gas constant, $T$ is temperature, and $n$ is the molar sum of all gases. This first term describes how the flux changes the bubble molar content and hence the change in bubble size with time ($t$). The second term describes how changes in hydrostatic pressure as the bubble rises (i.e., depth ($z$) decreases) affects bubble size, and depends on water density ($\rho_W$) and gravity ($g$). The denominator also includes the effect of surface tension ($\alpha$) on pressure – higher pressure implies a smaller bubble.

Unfortunately, bubble size distributions were not measured, thus a typical minor bubble size distribution from the literature was used. Implications of these simplifying assumptions are discussed in Section 4.4.

12

1  The model was initialized with a typical (Leifer, 2010) minor Φ (**Fig. 5a**) for either methane or nitrogen

2  bubbles, dissolved air gases at equilibrium in the water column, the observed CTD profile (**Fig. 5b**), and a

3  10 cm s$^{-1}$ upwelling flow ($V_Z$). $V_Z$ is an average value that is too low for the highest calibration flow and

4  too high for the lowest (Leifer, 2010).
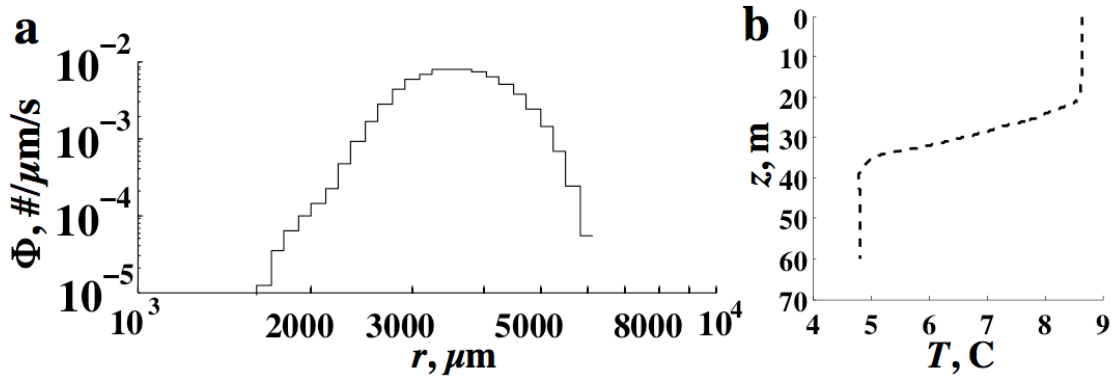


5
6  **Figure 5. a.** Minor bubble plume size distribution (Φ) with respect to equivalent spherical radius (*r*) used

7  to initialize the bubble model. **b.** Measured temperature (*T*)-depth (*z*) profile used in model.
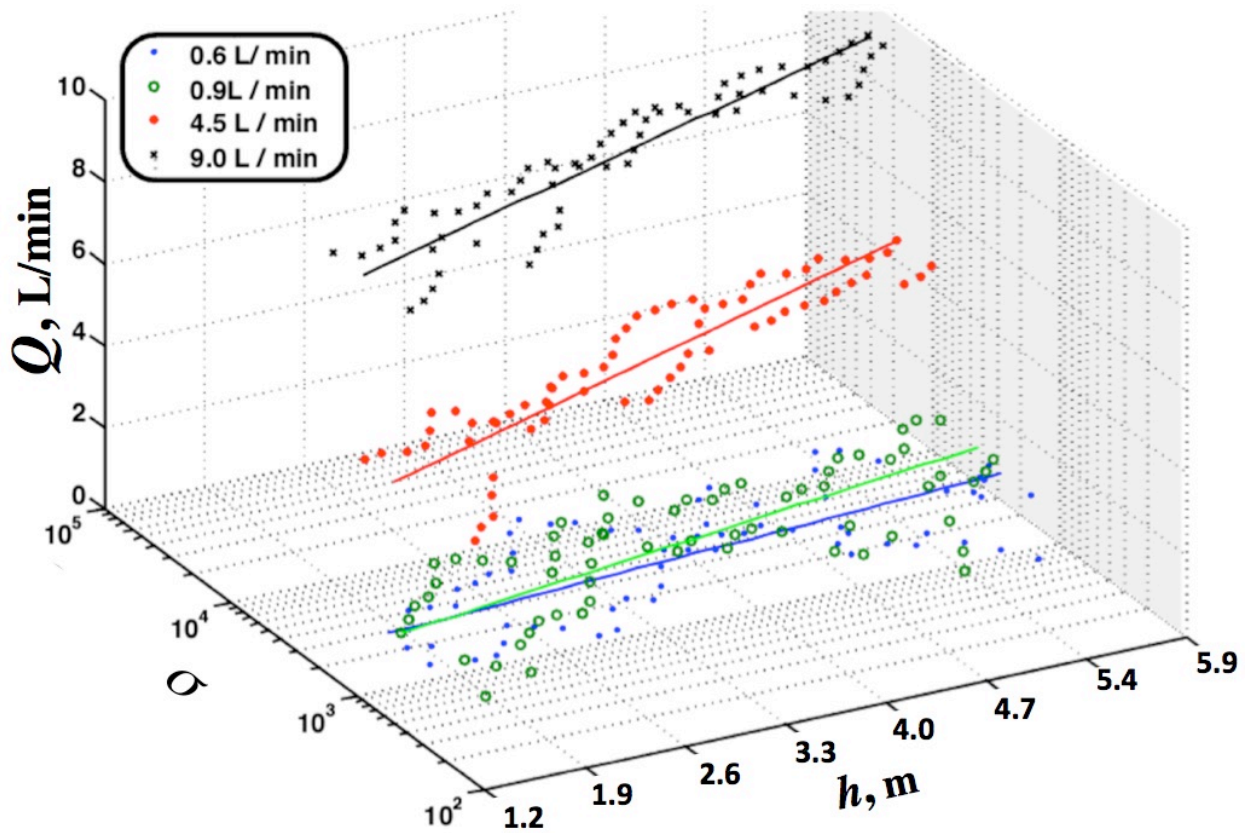


8
9  **Figure 6.** Field sonar data from the Coal Oil Point seep field for air bubbles in 22-m deep water. Sonar

10  return counts integrated across the plume, σ, versus airflow, *Q*, and height above seabed, *h*, for four

11  airflows and least-squares linear-regression fits to log(σ) versus *h*.

1  **3. Results**

2  **3.1. Engineered bubble plumes**

3  Sonar return for the two (high and low) calibration plumes (**Supp. Fig. S2**) was thresholded

4  above background (bubble-free water) and integrated for each beam during rotation across each

5  calibration plume. The thresholded $\sigma$ in a depth window then was fit with a linear polynomial of

6  the log of the integrated sonar return over the plume versus height, $h$. As the bubble plume rose,

7  $\sigma$ increased – i.e., $\sigma(h)$ was not constant (**Fig. 6**). Note, the change in volume for air bubbles over

8  such short rise heights is negligible. This is evidence of bubble-bubble acoustic interaction

9  decreasing as the bubbles rise and spread from turbulence (acoustic interactions decrease towards

10  zero as the inter-bubble distances increases to large distances). Note, these data were

11  uncalibrated and cannot be directly compared to the Arctic calibration data; it is presented to

12  show the depth trends.

13  There is significant geometric uncertainty in SBES data, which is evident in the overlap in time of sonar

14  returns for the calibration bubble plume (**Supp. Fig. S4**). This overlap results from current advection of

15  the plume orthogonal to the page. MBES addresses this SBES deficiency. For example, the SBES sonar

16  loses the bubble plumes once they have rose into the WML, where currents often shift, but the MBES

17  continues to observe them to 13-m depth, slightly below the vessel's draft.

18  The most common sonar return ping element is noise, which was isolated from the bubble-plume signal

19  based on setting a threshold from the sonar return probability distribution function ($\Psi(\sigma)$) at

20  approximately – 80 db (**Fig. 7a**). $\Psi(\sigma)$ weaker than -70 db is clearly distinct from the stronger, but less

21  common (lower $\Psi$), bubble $\Psi(\sigma)$. Based on inspection of $\Psi(\sigma)$, a noise threshold value of -70 db was

22  selected (**Fig. 7a**, arrow), which provided a 5-8 db transition between noise and bubbles. Obvious sonar

23  artifacts, which can exhibit strong sonar return signatures, were masked by spatial segregation.

24  Specifically, the plume center was identified at each depth and then filtered to ensure continuity with

25  depth. Then, only samples within a specified horizontal distance from the plume centerline that tightly

26  constrained the plume above the noise threshold were incorporated into the analysis.

27  For the engineered bubble plume experiments, plumes with volume flux ($Q$) from 0.019 to 1.1 L/s were

28  created and observed by both SBES and MBES systems (**Fig. 7**). The contribution of bubble plume weak

29  and strong sonar returns were investigated by their signature in $\Psi(\sigma)$. Specifically, $\Psi(\sigma)$ was modeled by

30  a piece-wise least-squares, linear-regression analysis of $\Psi(\sigma) = a\sigma(z)^{b}$. This model then was compared to

14

1    expected trends in plume evolution of a rising bubble plume. Fit parameters are shown in **Supp. Table**

2    **S1**. Example data and fits for the 0.8 L/s plume shown in Figs. 9d-9f for three depth windows (all below

3    the WML).
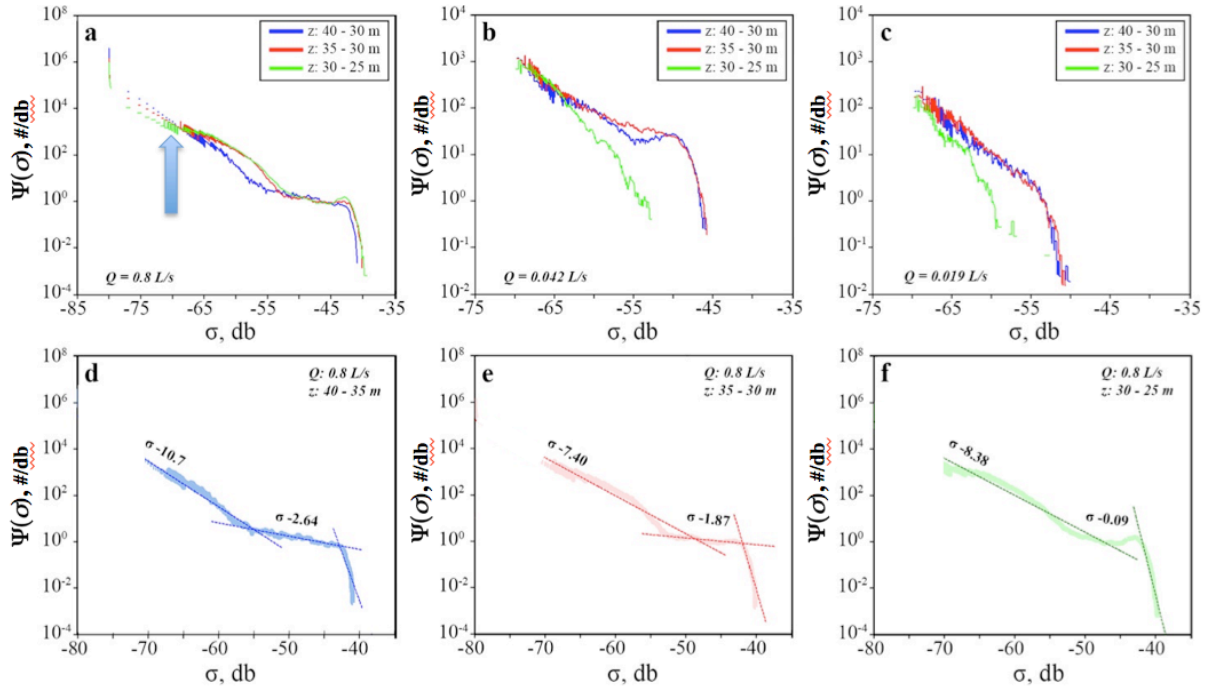


4

5    **Figure 7.** Plume-integrated sonar return ($\sigma$) occurrence probability distribution function ($\Psi(\sigma)$)

6    normalized to sonar bin-width (sonar bins are logarithmically spaced) for **a.** full water-column for a flow

7    ($Q$) of 0.8 L/s – unthresholded for processed depth windows, $z$, arrow shows noise threshold.

8    $\Psi(\sigma)$ thresholded for **b.** $Q$ = 0.042 L/s, **c.** 0.019 L/s and with linear fits for $Q$ = 0.8 L/s for **d.** $z$ = 35-40 m,

9    **e.** 30-35 m, **f.** 25-30 m. Data key on figure. Fit parameters in **Supp. Table S1**.

10   For low versus high flow plumes, $\Psi(\sigma)$ was distinctly different while $\Psi(\sigma)$ for the intermediate-flow

11   plume exhibited characteristics of both low and high flows. A weak $\sigma$ represents small bubbles, while

12   strong $\sigma$ may reflect large bubbles or dense aggregations of small and/or large bubbles. As a bubble

13   plume rises, the relative importance of small bubbles should increase as small bubbles disperse, spreading

14   the weak sonar return over a larger volume. $\Psi(\sigma)$ at the deepest depth for the weakest bubble plume

15   exhibits a clear, two-part power law (**Fig. 7c**; **Supp. Table S1**) and remained constant as the bubble

16   plume rose for the first 10 m, abruptly steepening in the next 5 m. This emphasizes the importance of

17   smaller bubbles ($b$ = -8, -7, -12 for weak $\sigma$ for the 45-40, 40-35, 35-30 m depth windows, respectively).

18   For the weaker bubble plumes (0.042 and 0.019 L/s, **Figs. 7b and 7c**, respectively), the strongest $\sigma$

19   disappear completely at the shallowest depth, consistent with bubble-plume dispersion, bubble

20   dissolution, and strong currents.

15

1    $\Psi(\sigma)$ is bi-modal for the deepest depth window for the highest-flow plume (**Fig. 7d**) with stronger $\sigma$ more

2    common relative to weaker $\sigma$ than in the low flow plume (**Fig. 7c**) and more common than "predicted" by

3    extrapolating the weak $\sigma$ power law fit ($\sigma^{-10.7}$) to stronger $\sigma$ (**Figs. 7d and 7f**, respectively). As this plume

4    rose, $\Psi(\sigma)$ for weak $\sigma$ decreased in relative importance while $\Psi(\sigma)$ for stronger $\sigma$ remains constant – the

5    power law exponent for the intermediate depth ($b=-7.4$) was less steep than for deeper (-10.7) and

6    shallower (-8.4) depths. Thus, most of the evolution of $\Psi(\sigma)$ is from spatial expansion of weaker $\sigma$, i.e.,

7    smaller bubbles, while the denser, strong $\sigma$ bubbles remain relatively uniformly constrained with depth.

8    The overall increase in $\sigma$ with rise is the same character observed in the precursor COP study (**Fig. 6**),

9    which featured strong plumes comparable to the strong plumes in **Figs. 7d-7f**.

10   $\Psi(\sigma)$ for the intermediate flow plume (**Fig. 7b**) shares characteristics of both the high and low flow plume

11   $\Psi(\sigma)$, bi-modal at the deepest depth with a pronounced strong $\sigma$ peak in $\Psi(\sigma)$ (like the high flow plume)

12   evolving into a dual power law as the plume rises – as for the low flow plume $\Psi(\sigma)$. Thus, $\Psi(\sigma)$ for the

13   intermediate flow plume evolved as it rose through the patterns of the strong to weak flow plumes.

14   These are point source plumes that disperse as they rise, thus bubble-bubble multiple scattering should

15   decrease with height. With the exception of the strongest plume, plume rise decreases $\sigma$; however, for the

16   strongest flow plume, rise initially increases $\sigma$, similar to the behavior in the precursor study (**Fig. 6**),

17   which was for comparably high flows, albeit over depths much closer to the source. See **Supp. Figs. S5**

18   **and S6** for example MBES data for these flows.

19   The depth-dependent calibration curves ($\sigma(Q,z)$) were derived to account for the depth-evolving bubble-

20   bubble acoustic interactions as the bubbles rose (**Fig. 8**). Specifically, $\sigma$ above the noise threshold in

21   spatially segregated boxes in each depth window is averaged over 7-minutes of sonar data for each flow

22   to derive $\sigma(Q,z)$. The MBES and SBES calibration datasets show saturation at high flow, similar to

23   Greinert and Nützel (2004), which is evidence of bubble-bubble multiple scattering as shown in

24   simulations by Weber (2008). For the high flow cases, this likely includes sonar shadowing of more

25   distant bubbles by nearer bubbles (decreasing $\sigma$). At low flow, $\sigma$ increases with increasing $Q$ far faster

26   than linear addition of the number of bubbles. For example, for a flow doubling ($Q=0.02$ to 0.04 L/min),

27   $\sigma$ should increase $20\log_{10}(2)$, or 6 db, yet increases are much larger.

28   $\sigma(Q,z)$ shows a depth dependency in $\sigma$ for both SBES and MBES systems (**Fig. 8**). For low flow plumes,

29   $\sigma$ decreases with rise and is non-linear with $Q$. In contrast, for high flows, both SBES and MBES saturate

30   or are near saturation although there is significantly more variability in the MBES data. Saturation occurs

31   when increased $Q$ has minimal to no increase in $\sigma$. Close inspection of the high-flow plume MBES data

revealed undulations, which may have led to depth aliasing of σ in the 5-m depth windows. Although the high flow calibration plumes are relevant for major seep bubble plumes such as in COP seep field (Leifer, 2010); the ESAS plumes studied were weaker. Thus, the strong calibration plumes are not discussed further. In contrast, the low flow calibration plumes are comparable to typical minor bubble plumes (Leifer, 2010) and span the observed range of natural seepage in the study area.
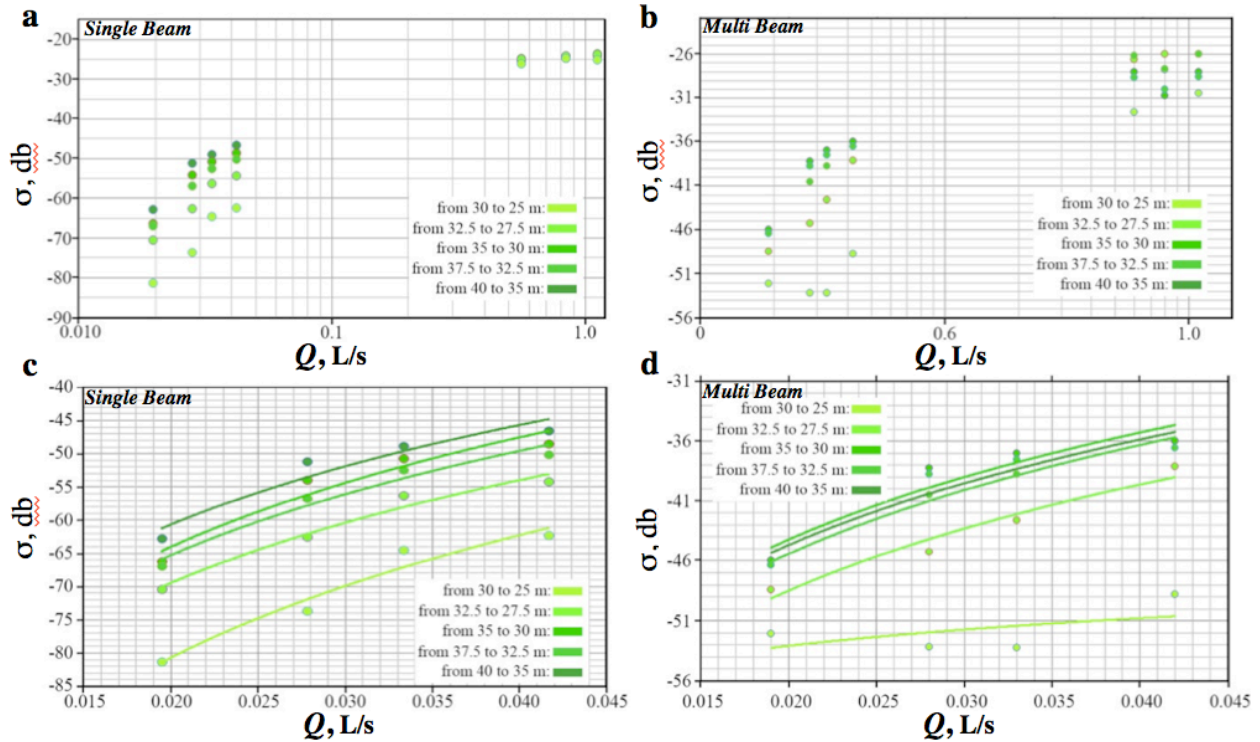


**Figure 8.** Sonar return (σ) versus volumetric flow ($Q$) calibration curves for the single-beam sonar for **a** all $Q$ and for **c** low $Q$, and for the multibeam sonar for **b.** all $Q$ and for **d.** low $Q$. Fit parameters are shown in **Supp. Table S2**.

### 3.2. Bubble Dissolution Rates and Volume Flux

These *in situ* σ($Q,z$) were derived for application to seep bubble sonar survey data, and accounts for the bubble vertical velocity from buoyancy and upwelling flow. However, application of σ($Q,z$) should account for the depth difference between the seep study area and the calibration plumes (70 versus 40 m) and different gas composition – seep gas primarily is $CH_4$, while the calibration gas was nitrogen. Both these factors have non-negligible implications for the bubble dissolution rates of the two different plumes.

These differences cause different bubble plume evolution and thus different volume height profiles. A volumetric correction factor was developed based on the ratio of the volume height profiles between a

17

1 calibration and a seep bubble plume (same bubble size distribution) based on numerical bubble
2 propagation model simulations (**Fig. 9**).
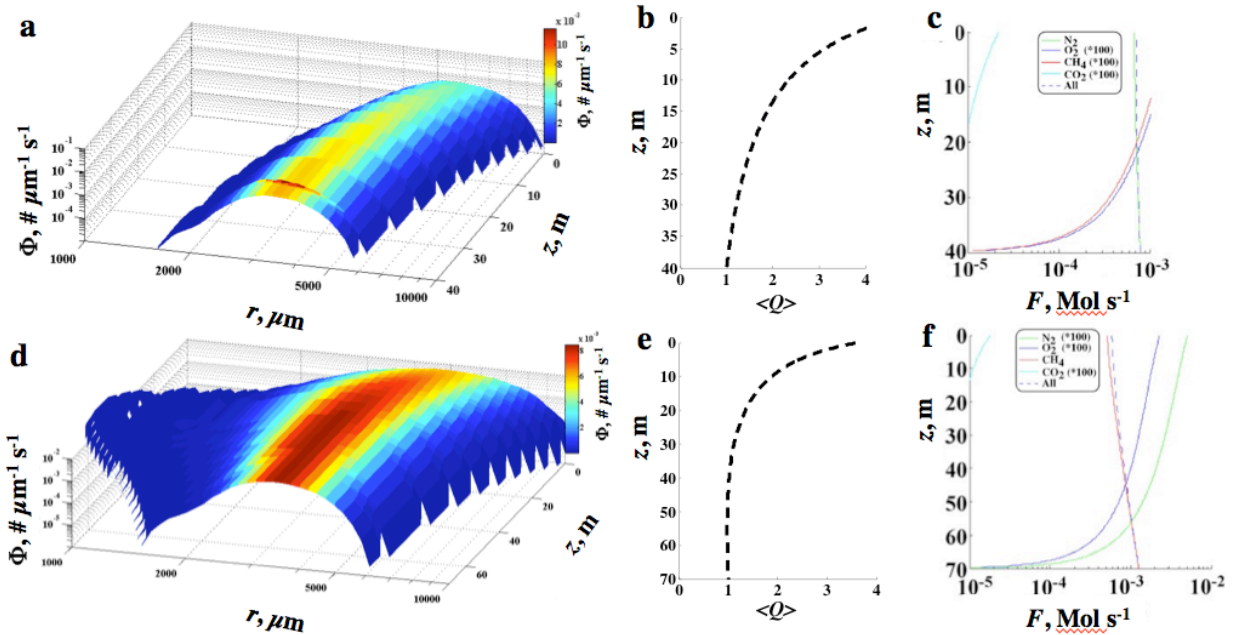


4 **Figure 9. a.** Depth ($z$) evolution of the bubble plume size distribution ($\Phi$) for a nitrogen minor plume
5 (calibration) from 40 m and **d.** for a $CH_4$ seep plume from 70 m. Seabed normalized volume averaged
6 over depth window ($<Q>$) of the rising bubble plume for **b.** calibration plume, and **e.** seep plume. Molar
7 vertical flux for **c.** calibration plume, and **f.** seep Data keys on panels.

8 The numerical simulations show that for the first three, 5-meter depth windows, the depth-averaged total
9 bubble plume volume ($<Q_z>$) increases by 4.7%, 15%, and 29%, respectively (**Fig. 9b**). This growth
10 occurs from decreasing hydrostatic pressure (primarily) and from oxygen inflow (secondarily), while it
11 shrinks from nitrogen outflow. Growth indicates the balance favors hydrostatic over nitrogen outflow.

12 The size distribution of a minor seep bubble plume changes dramatically as it rises from 70-m depth with
13 the smallest bubbles dissolving and the largest bubbles growing (**Fig. 9d**). Overall, air uptake and
14 decreasing hydrostatic pressure largely balance dissolution for the first 50 m of bubble rise and $<Q_z>$
15 remains roughly stable (**Fig. 9e**) – $Q$ decreases by 0.7%, 0.2%, and 0.0% in the first three 5-meter depth
16 windows, respectively. Note, stable $Q$ does not imply constant total $CH_4$ bubble content, which
17 continually outflows the rising bubble.

18 Combining the volumes from the two simulations provides the volume correction factors, 0.948, 0.868,
19 and 0.775 for the 65-70, 60-65, and 55-60 m depth windows, respectively. Thus, the calibration plume $Q$

1 averaged over the 35-40 m depth window is ~5% greater than the seep bubble plume $Q$ for the 70-65 m

2 depth window.

3 **3.3. Natural Seepage**

4 The calibration $\sigma(Q,z)$ was applied to MBES and SBES Laptev Sea sonar data under conditions of strong

5 currents. Flux for the seep areas (**Fig. 10**) was mapped by averaging the seepage flux in the 65-70 m

6 depth window in 1-m$^2$ quadrats after application of the calibration curves and correction factors. The

7 deepest depth window was chosen to preserve better the seabed location of emissions for spatial analysis.

8 Three seep areas were surveyed, two weak and one strong, all with numerous plumes. The MBES data

9 illustrates the additional spatial information missing in SBES systems. For example, Seep Area 1 in the

10 SBES data (**Fig. 10b**) appears to show extensive diffuse seepage, which the MBES data (**Fig. 10a**) reveal

11 arises from many low-flow discrete bubble plumes.
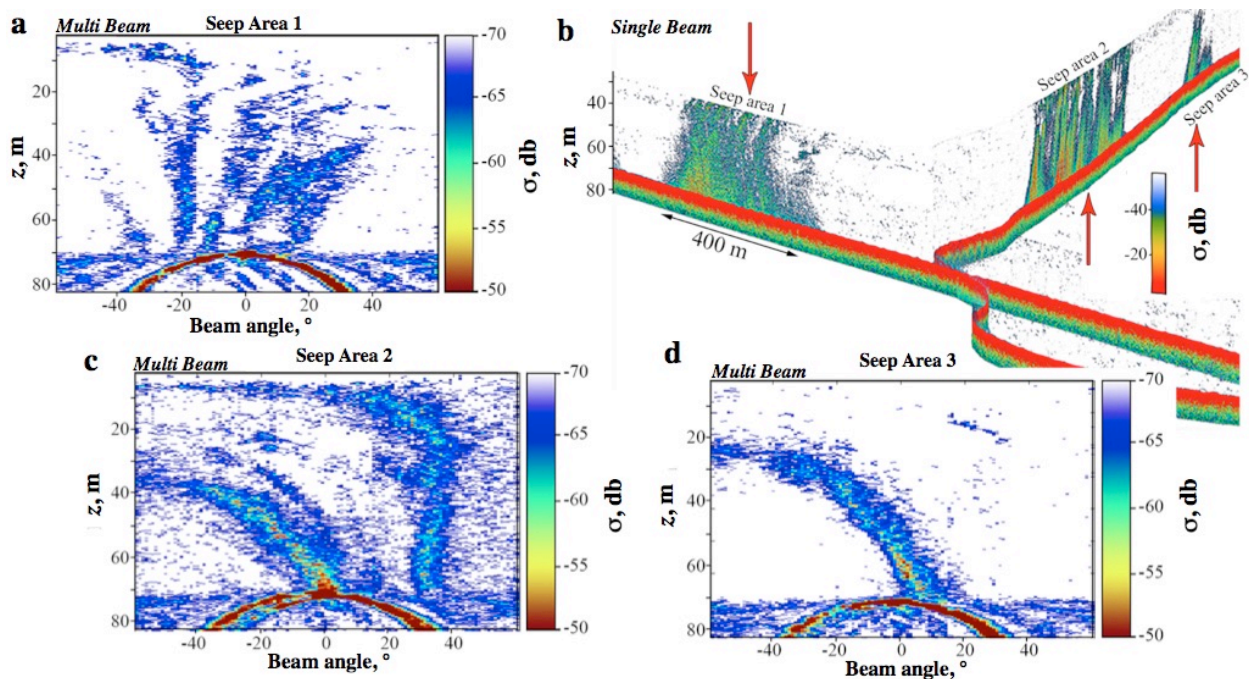


12
13 **Figure 10.** Sonar return, s, with depth, $z$, of seep bubble plumes in the Laptev Sea. **a. c. d.** Multibeam

14 sonar data, single ping, in each of the seep areas, locations labeled on b. **b.** Single beam sonar data. Size

15 scale and data key on panels.

16 Seep Area 2 was stronger than the other seep areas by an order of magnitude and clearly showed a

17 northeast-southwest trend, which is apparent in all seep areas. Some of the striation patterns, primarily of

18 the weaker returns, are consistent with the very strong currents detraining small bubbles out of the plume

19 in the direction of the sonar beam fan. On a second, east-west leg, Seep Area 1 was surveyed with

20 currents not aligned with the sonar beam fan and does not exhibit striation. Further evidence of the effect

19

1 of currents is shown in the sonar ping data (**Fig. 10b vs. Figs. 10c and 10d**); where Seep Area 1 does not

2 show the extreme tilt across beams as in sonar data for Seep Areas 2 and 3. Thus, the linear seep trends

3 reflect geological control.

4 Seepage spatial structure showed numerous seeps clustered around the strongest seep with an apparent

5 modulation at distances of ~100 m (**Supp. Fig. S7**). The dominant plumes in Seep Areas 1 and 3 were as

6 strong as 0.3 mmol m$^{-2}$ s$^{-1}$ (7.4 cm$^3$ s$^{-1}$) while the dominant seep plumes in the larger Seep Area 2 (**Fig.**

7 **11c**) released >0.6 mmol m$^{-2}$ s$^{-1}$ (15 cm$^3$ s$^{-1}$).
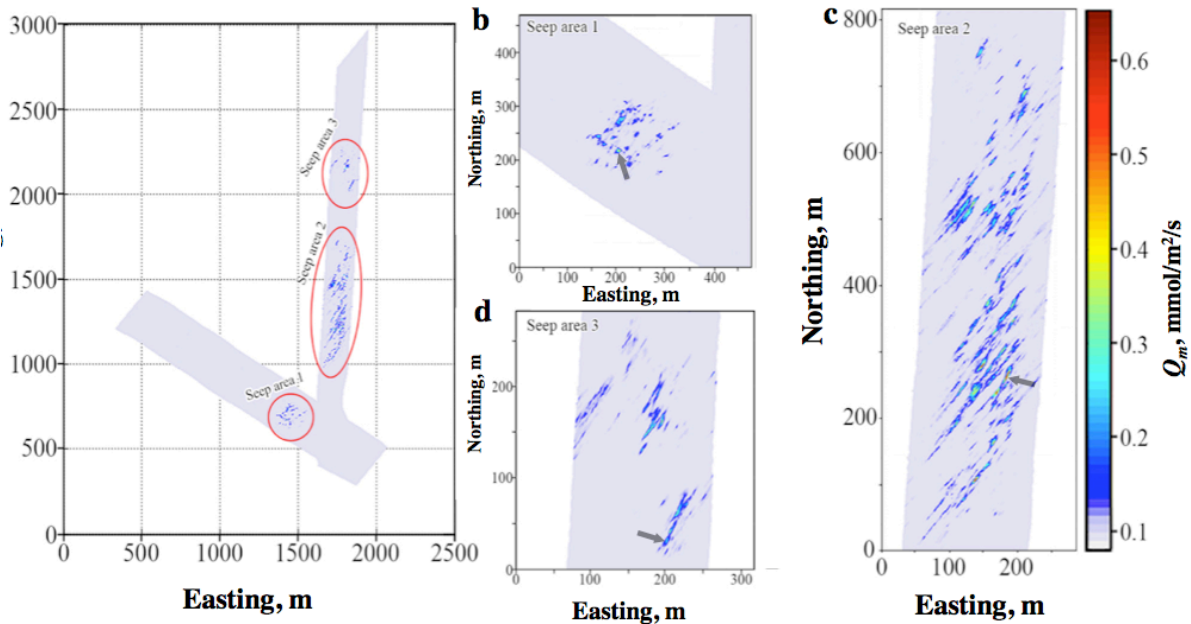


8
9 **Figure 11.** Seep mass flux ($Q_m$) map for **a.** all seep areas, and for **b-d.** Seep Areas 1-3. Data key on panel

10 c. Fits in Table 2.

11 The mass flux ($Q_m$) occurrence probability distribution function ($\Psi(Q_m)$) was calculated for each seep

12 area and showed Seep Area 2 contained the largest number of strong seep plumes followed by Seep Area

13 3 and then Seep Area 1 (**Fig. 12**). For the seep areas, $\Psi(Q_m)$ for weak emissions asymptotically

14 approached ~0.1 mmol/m$^2$/s (2.5 cm$^3$/s) for all seep areas–the noise level. Thus, calibration flows (**Fig. 8**)

15 bracketed from MBES data from the noise floor to the largest observed seep plume.

16 Seep Area 2 exhibits both greater fluxes and a shallower power law than other seep areas (**Fig. 12c**).

17 Furthermore, all seep areas exhibited positive anomalies or peaks in $\Psi(Q_m)$ for stronger flux seepage.

18 These peaks signify a preferred emission mode–i.e., multiple seeps with similar emission fluxes. For

19 weaker seeps with good signal to noise ($Q_m$ >0.15 mmol/m$^2$/s), the power law fits are nearly identical,

20 6.65, 6.27, 6.80 for Seep Areas 1, 2, 3, respectively (**Table 2**).

20
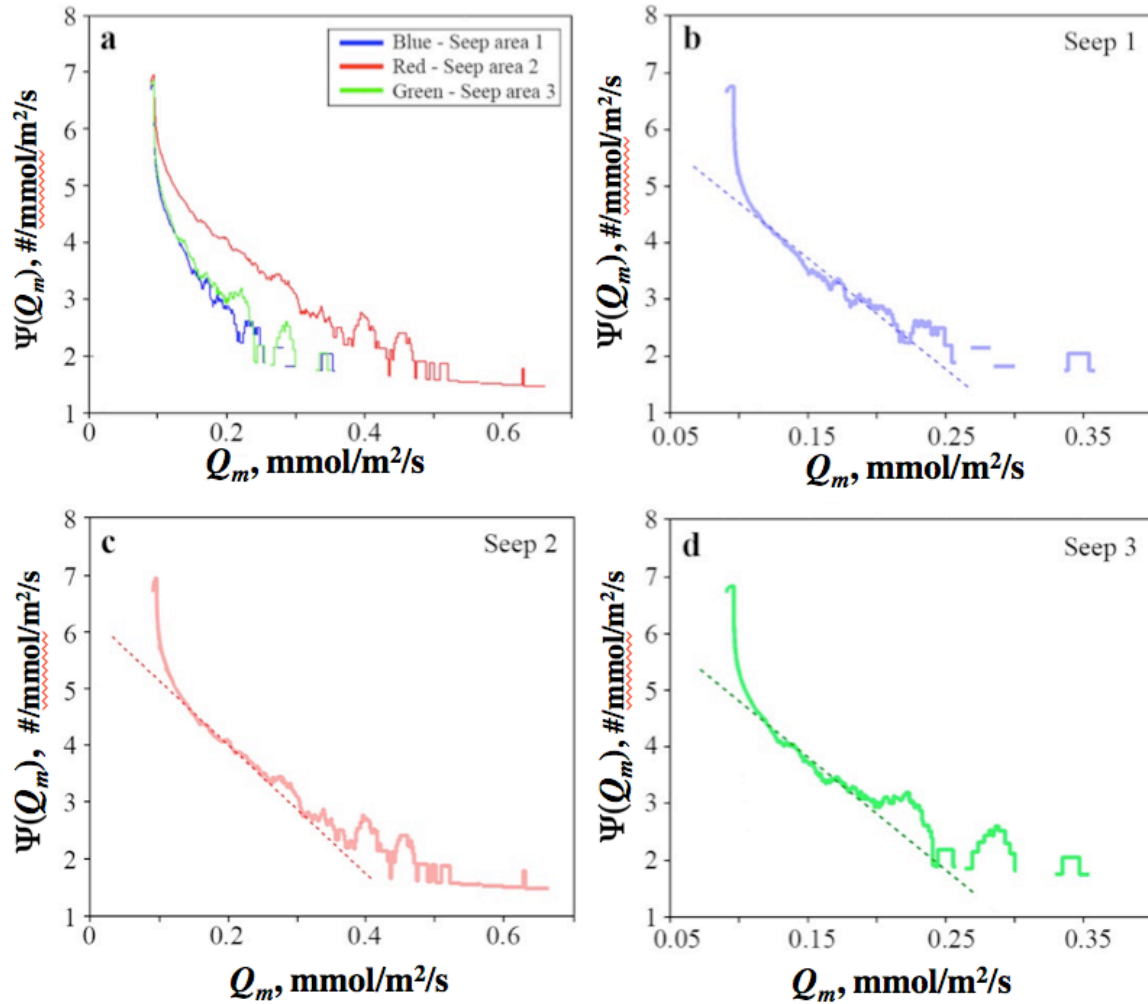
**Figure 12.** Seep mass flux ($Q_m$) occurrence probability distribution function ($\Psi(Q_m)$) normalized to flux bin-width (bin widths are logarithmically-spaced) for **a** all seep areas, and for **b-d** Seep Areas 1-3 with power law fits. Data key on panel a. Fits in Table 2.

Total flux in each seep area was determined by area integration and was 5.56, 42.73, and 4.88 mmol/s for the MBES data (**Table 2**). SBES-derived emissions were biased lower compared to MBES, by 3.7% to 36% for the seep areas, with best agreement for Seep Area 2.

TABLE 2 HERE

## 4. Discussion

### 4.1. Bubble-Bubble Acoustic Interaction

We presented results of an *in situ* engineered bubble plume experiment to investigate the evolution of bubble plume sonar return for flows spanning two orders of magnitude. This range was comparable to

21

typical low flow minor plumes and very strong high flow major plumes (Leifer, 2010). Calibration plume sonar return increased strongly and non-linearly with flux, ~15 db for a flow doubling from 0.02 to 0.04 L/s. This increase is faster than the 6 db increase that would be expected by simply summing the sonar cross sections of the doubled number of bubbles. Instead, the increase suggests strong bubble-bubble acoustical interactions. Specifically, with increased flow, overall plume dimensions expand more quickly, leading to less bubble shadowing and shallower sonar occurrence probability distribution function slopes at the same height above the nozzle (**Fig. 7**). In contrast to the overall plume dimensions (which includes smaller more dispersed bubbles), the dense core of large bubbles tends not to disperse and is largely insensitive to height (**Fig. 7**). Thus, for the dense core, increased flux increases bubble shadowing (multiple scattering) such that the signal of the additional bubbles is blocked by other bubbles and sonar return becomes nearly independent of flow, i.e., saturated (**Figs. 8a and 8b**). Similar saturation is apparent in the data presented in Greinert and Nützel (2004) for an air bubble plume in far shallower water. Thus, the calibration data provides strong evidence of non-negligible bubble-bubble acoustical interaction at both low and high flow rates. Furthermore, the relationship's non-linearity is shown in the trend of $\sigma(z,Q)$ as the bubble plume rises and disperses. Thus, bubble multiple scattering is significant even after the plume has risen 15 m.

As a high-flow bubble plume rises, the weak $\sigma$ portion of the plume representing small bubbles dispersed, leading to an increase in the integrated $\sigma$ as was observed in the Coal Oil Point (COP) and ESAS engineered plume data. In the COP seep field study, calibration flows extended from comparable to far higher flows than those in the ESAS and documented that $\sigma(z)$ increased with height on fine depth scales (**Fig. 6**). This was interpreted as due to decreasing bubble "shadowing" of more distant bubbles as the plume expands and becomes more diffuse during the plume growth or acceleration phase (Leifer et al., 2015a). As the ESAS calibration plumes rose, the sonar occurrence probability distribution function showed a strong influence from small bubble dispersion as the plume expanded and an increase in the integrated $\sigma$ (**Fig. 8**)

As low-flow calibration plumes rise and disperse, $\sigma$ decreases. Overlapping intermediate depth windows were evaluated and confirmed this was not an artifact of plume oscillatory motions aliasing the return signal across the depth windows. The decrease in integrated $\sigma$ with rise is (by definition) a decrease in scattered sonar energy, i.e., greater energy scatters back to the sonar when the plume is spatially denser. This could arise from a decrease in shadowing from scattering, or dissolution; however, the bubble model showed that minor plume dissolution did not change overall plume volume significantly (**Fig. 9**), unlike the significant changes in integrated $\sigma$, e.g., **Fig. 8c**.

**4.2 Bubble Detrainment and Bubble-Bubble Acoustic Interaction**

The artifact striations in the natural seep sonar data from currents are consistent with non-negligible bubble-bubble acoustic interaction (**Fig. 11**). Specifically, seep bubble plumes were imaged for high currents that advected small bubbles out of the plumes into the downcurrent water. When detrained bubbles were in the beam fan orientation, they were observed, but not when the beam fan was perpendicular to the currents. For co-orientation, scattered acoustic energy interacts with nearby downcurrent bubbles, which remain in the beam. This arises because the cross-track beam dimension is very broad (120°), while the along-track beam width is very narrow – a few degrees. Thus, when cross-oriented, the sonar beam fan fails to image detrained bubbles. This provides clear evidence of bubble-bubble scattering at larger distances than the plume dimensions.

**4.3. Bubble Size Distribution**

Bubble size distributions have been reported for other ESAS seep sites (Shakhova et al., 2015), but equipment to make bubble measurements were unavailable for this study. Bubble modeling was used to address the effect of evolving bubble size distribution with flow in application of calibration air or nitrogen (preferred for safety reasons over methane) bubble plumes to seep bubble plumes (**Fig. 9**). Thus, we applied a first approximation using a typical minor bubble plume size distribution. Clearly initializing the model with measured plumes would improve the accuracy of the volume correction factor and hence sonar-derived flux. Still, the primary goal in our study is to demonstrate with a simple approximation that bubble size matters and should not be neglected.

Although the simulations were conducted to correct between a nitrogen calibration plume and pure methane seep bubbles, if the seep bubbles contained other gases at non-trace levels, their outgassing could impact significantly bubble size evolution. In particular, $CO_2$, which is far more soluble than $CH_4$, can lead to rapid bubble size change, primarily in the deepest depth windows, e.g., see $CO_2$ plume simulation in Leifer et al. (2015b). Additionally greater sensitivity arises from bubble plume depth (Leifer and Patro, 2002). Thus, the depth discrepancy between calibration and seep plumes should be minimized. Future calibration studies also should account for size distribution and upwelling flow with respect to flow rate.

**4.4. Field comparison of MBES with SBES**

The MBES and SBES systems were calibrated with the same nitrogen gas bubble plumes, thus the two systems should agree in terms of flux observations. Calibration flows spanned very weak flow ($Q = 0.19$ L/s) to very strong flows ($Q = 1.1$ L/s). The low-flow calibration bubble plume (**Fig. 8**) was less than the seep field noise floor of the MBES system (**Fig. 12a**). In contrast, the high flow calibration bubble plume was more than an order of magnitude greater than field observations.

23

1   Field observations showed far better agreement between systems for Seep Area 2 than the other seep

2   areas (**Table 2**). This most likely relates to the greater relative importance of stronger seeps that are well

3   above the noise level relative to the other seep areas. The calibration flows (**Fig. 8**) showed weaker sonar

4   return for the SBES than for the MBES for the same flow. Geometric uncertainty likely played a role in

5   the SBES downward bias.

6   **4.5. Seepage Spatial Characterization**

7   The seepage spatial map in the ESAS (**Fig. 11**) share similarities with spatial patterns in the COP seep

8   field (**Fig. 1**). Subsurface geologic structures control the seepage spatial-flux distribution by creating the

9   pathways through which seepage migrates to the seabed and ocean - seepage areas must occur where

10  geologic structures allow. In the COP seep field, strong seepage areas are located at intersecting non-

11  compressional faults and fractures (Leifer et al., 2010). Furthermore, these faults and/or fractures

12  themselves are preferred migration pathways that connect subsurface reservoirs to the seabed, with

13  seepage tending to manifest along their trend.

14  Two spatial trends were manifest in the ESAS seepage map (**Fig. 11**), one northeast-southwest of

15  individual vents and second a north-south elongation in Seep Area 2. Both trends were aligned with the

16  two weaker seepage areas. Furthermore, the northeast-southwest trend is apparent within Seep Area 2.

17  Here, fractures in submerged permafrost could play a similar role to the role of fault intersections in the

18  COP seep field; however, more extensive seep area mapping is needed for validation, and/or penetrating

19  sonar data that can image near surface rock strata. On smaller length scales, there is an evident striation

20  pattern in vent locations suggesting a subsurface linear geological control on meter length scales.

21  High flow seepage requires high permeability migration pathways, while low flow seepage occurs along

22  low permeability migration pathways if the driving pressure between the deeper reservoir and the seabed

23  is constant across the active seepage area (Leifer and Boles, 2005). Thus, the stronger and more numerous

24  and extensive seepage emissions from Seep Area 2 indicates higher subsurface permeability and

25  subsurface connectivity with more numerous migration pathways than the other seep areas (**Fig. 11**).

26  Seepage connectivity can be envisioned topologically as an inverted branched structure (Leifer and Boles,

27  2005) where central stronger seepage is surrounded (generally) by weaker seepage (**Supp. Fig. S7**).

28  Given that permeability is inversely related to resistance in the migration pathways, stronger seepage is

29  fed by migration along pathway(s) with lower resistance (higher permeability), while weaker seepage is

30  fed by migration along pathways with stronger resistance (lower permeability). The balance between

31  seepage emissions for different migration pathways with a range of permeability underlies the flux

32  probability distribution function (**Fig. 12)**.

24

1   The seepage emissions map demonstrates similar geologic spatio-flux control. Specifically, weak seepage

2   exhibited a *b*=-6 power law (**Fig. 11**), which describes the distribution between high and low permeability

3   migration pathways. This argues that the shallow seabed structure (fracture, porosity, etc.) related to low

4   permeability migration pathways is common across the areas, with the main controlling factor being the

5   number of bubbles escaping per second per unit area of seabed. Note, although *b* is affected by bubble

6   detrainment into the beam fan for Seep Areas 2 and 3, Seep Area 1 does not exhibit this effect, yet has

7   similar *b*.

8   This power law does not extend to the largest seep fluxes, which manifest as peaks in the flux probability

9   distribution function. Thus, higher flow plumes could represent normal seabed structure failure (that

10  governs the weak seepage) from stresses and/or talik melting, leading to focused high flow migration

11  pathways that help define where the seep areas lie.

12  In the Arctic, subsea permafrost degradation from heating both below (geologic – most strong in faulted

13  zones) and above (riverine inputs and overall Arctic Ocean warming) creates migration pathways that

14  manifest as seep spatio-flux distributions. The presence of active seepage in this region likely relates to

15  these heat flows, with the hotspots likely related to taliks and/or subsea thaw lakes, whose locations are

16  controlled by linear geologic structures. In the ESAS, grabens are often linear structures, which often are

17  correlated with paleo-river valleys, and could cause co-aligned fractures controlling seepage along linear

18  trends. The similarity in the emission probability distribution power laws between seep areas indicates

19  that subsurface permeability exhibits similar fractal distribution between the three areas. This argues for

20  similar formation mechanism, i.e., taliks. In this case, at the intersection of the two linear trends, where

21  fluid migration thus heat flow likely are higher, leading to more rapid talik development providing high

22  permeability migration pathways.

23  **4.6. Broader Implications**

24  There are enormous carbon stores sequestered in marine-permafrost in the Arctic, which are of particular

25  concern for release as the warming Arctic Oceans transfer heat faster than from the atmosphere to

26  terrestrial permafrost. Migration from this submerged permafrost reservoir to the ocean has created a vast

27  marine seep field that lies entirely in shallow waters with emissions contributing directly to atmospheric

28  budget (Shakhova et al., 2014). Widespread ESAS seabed bubble emissions have been documented

29  (Shakhova et al., 2014; Shakhova et al., 2015), demonstrating permafrost integrity failure that makes $CH_4$

30  and additional organic carbon available for microbial $CH_4$ generation.

31  These observations support the hypothesis that the sub-sea permafrost is a controlling factor to spatial

32  variability in seabed $CH_4$ fluxes. The current state of subsea permafrost is key to understanding how $CH_4$

25

in ESAS seabed reservoirs escapes to atmosphere. There is enormous uncertainty in future emissions largely due to the paucity of data. *In situ* calibrated sonar shows significant promise as a new tool to evaluate quantitatively seabed fluxes over wide areas.

**4.7. Future Directions**

In this study, bubble plume spanning almost two orders of magnitude flow (0.019 to 1.1 L/s) were studied; however, a key intermediate range (0.045-0.8 L/s) was missed. These bubble plumes are in the transition from a non-linear relationship between σ and flow to saturation where σ is largely independent of flow. Future experiments should endeavor to follow plumes for more than 15 m; however, currents made this infeasible. Given that seep bubble plumes often escape from nearby vents into plumes that eventually merge and the importance of bubble-bubble acoustic interactions, calibration studies should include multiple bubble plumes from closely located sources. Studies in calmer waters could elucidate better the importance of small bubbles versus large bubbles to overall sonar return.

This study featured the novel use of a numerical bubble plume model to correct for different size evolution between calibration gas bubble plumes and seep bubble plumes. Uncertainty arises from the bubble size distribution, which needs to be measured for the calibration and seep bubble plumes at multiple flow rates. Our approach was a simplified first effort with room for improvement.

**5. Conclusions**

In this study, we present a methodology of using *in situ* plume calibration approach to derive quantitative sonar methane emissions. We created *in situ* engineered bubble plumes from 40-m depth spanning almost two orders of magnitude flow (0.019 to 1.1 L/s). Non-linear calibration curves related sonar return to flux for a range of depths and demonstrated significant bubble-bubble acoustic interactions, precluding an inversion approach based on scaling bubble sonar cross section with the (unmeasured) size distribution. Weak sonar occurrence probability distribution function was well described by a power law that likely correlated with small bubble dispersion, while strong sonar returns largely were independent of depth, consistent with a focused central core of large bubbles.

The *in situ* calibration curve was applied to natural seepage from 70-m depth in the Laptev Sea outer shelf where subsea permafrost is predicted degraded in modeling studies. A correction then was made for the different volume evolution of the nitrogen calibration plume and the methane seep bubble plume through use of a numerical bubble plume model. The model was initialized with a typical (assumed) minor bubble plume size distribution and suggested ~5% correction for the first 5-m depth window. Emissions for three seepage areas of 5.56, 42.73, and 4.88 mmol/s were derived from multibeam sonar data, with good to reasonable agreement (4-37%) between single (biased lower) and multibeam sonar.

Seepage occurrence probability distribution function was bimodal, with weak seepage well described by a power law. This was interpreted as suggesting primarily small minor bubble plumes. Seepage mapped spatial patterns suggested subsurface geologic control along linear trends. The analysis showed show a probability distribution analysis could provide insights into geologic control.

## 6. Acknowledgements

**Tables**

**Table 1.** Integrated depth-windowed methane flux estimates.

| Designation | $Q_{m\text{-SBES}}$* | $SQ_{m\text{-SBES}}$ | $Q_{m\text{-MBES}}$** | $SQ_{m\text{-MBES}}$ | Area | $E$ | $SQ_{m\text{-MBES}}$ |
|---|---|---|---|---|---|---|---|
| | (mmol/m²/s) | (mmol/s) | (mmol//m²/s) | (mmol/s) | (km²) | (%) | (L/s) |
| Seep 1 | 0.22 | 3.78 | 0.33 | 5.56 | 0.017 | 32 | 0.14 |
| Seep 2 | 0.59 | 41.16 | 0.61 | 42.73 | 0.070 | 3.7 | 1.07 |
| Seep 3 | 0.26 | 3.96 | 0.33 | 4.88 | 0.015 | 19 | 0.12 |

$Q$ is volume flux, $Q_m$ is mass flux, U is uncertainty, where $E = (Q_{m\text{-MBES}} - Q_{m\text{-SBES}})/Q_{m\text{-MBES}}$

*SBES – Single Beam Echosounder, 65-70 m, depth window.

**MBES – Multibeam Echosounder, 65-70 m, depth window.

**Table 2.** Fit parameters for seep area flux probability distribution function.

| Name | $Q_{m-1}$* | $Q_{m-2}$ | a | b | $R^2$ |
|---|---|---|---|---|---|
| | (mmol/m²/s) | (mmol/m²/s) | (-) | (mmol/m²/s) | |
| Seep Area 1 | 0.1 | 0.2 | -19.53 | 6.648 | 0.836 |
| Seep Area 2 | 0.1 | 0.3 | -11.34 | 6.27 | 0.9228 |
| Seep Area 3 | 0.1 | 0.2 | -19.85 | 6.798 | 0.8258 |

Fit from $Q_{m-1}$ to $Q_{m-2}$, where $Q_m$ is the mass flux rate

**References**

Archer, D. and Buffett, B.: Time-dependent response of the global ocean clathrate reservoir to climatic and anthropogenic forcing, Geochem. Geophys. Geosyst., 6, Q03002,, 2005.

1  Bauch, H. A., Mueller-Lupp, T., Taldenkova, E., Spielhagen, R. F., Kassens, H., Grootes, P. M.,
2      Thiede, J., Heinemeier, J., and Petryashov, V. V.: Chronology of the Holocene transgression
3      at the North Siberian margin, Global and Planetary Change, 31, 125-139, 2001.
4  Biastoch, A., Treude, T., Rupke, L. H., Riebesell, U., Roth, C., Burwicz, E. B., Park, W., Latif,
5      M., Boning, C. w., Madec, G., and Wallman, K.: Rising Arctic Ocean temperatures cause gas
6      hydrate destabilization and ocean acidification, Geophysical Research Letters, 38, L08602,
7      2011.
8  Clark, J. F., Schwager, K., and Washburn, L.: Variability of gas composition and flux intensity in
9      natural marine hydrocarbon seeps. New Energy Development and Technology (EDT)
10     Working Paper 008, UCEI, 15 pp., 2005.
11 Clark, J. F., Washburn, L., Hornafius, J. S., and Luyendyk, B. P.: Dissolved hydrocarbon flux
12     from natural marine seeps to the southern California Bight, Journal of Geophysical Research,
13     105, C5, 2000.
14 Clift, R., Grace, J. R., and Weber, M. E.: Bubbles, Drops, and Particles, Academic Press, New
15     York, 1978.
16 Dickens, G. R.: Rethinking the global carbon cycle with a large, dynamic and microbially
17     mediated gas hydrate capacitor, Earth and Planetary Science Letters, 213, 169-183, 2003.
18 Drachev, S. S., Kaul, N., and Beliaev, V. N.: Eurasia spreading basin to Laptev Shelf transition:
19     structural pattern and heat flow, Geophysical Journal International, 152, 688-698, 2003.
20 Friedlingstein, P., Cox, P., Betts, R., Bopp, L., von Bloh, W., Brovkin, V., Cadule, P., Doney, S.,
21     Eby, M., Fung, I., Bala, G., John, J., Jones, C., Joos, F., Kato, T., Kawamiya, M., Knorr, W.,
22     Lindsay, K., Matthews, H. D., Raddatz, T., Rayner, P., Reick, C., Roeckner, E., Schnitzler,
23     K. G., Schnur, R., Strassmann, K., Weaver, A. J., Yoshikawa, C., and Zeng, N.: Climate–
24     carbon cycle feedback analysis: Results from the C4MIP model intercomparison, Journal of
25     Climate, 19, 3337-3353, 2006.
26 Gautier, D. L., Bird, K. J., Charpentier, R. R., Grantz, A., Houseknecht, D. W., Klett, T. R.,
27     Moore, T. E., Pitman, J. K., Schenk, C. J., and Schuenemeyer, J. H.: Assessment of
28     undiscovered oil and gas in the Arctic, Science, 324, 1175-1179, 2009.
29 Gramberg, I. S., Kulakov, Y. N., Pogrebitsky, Y. E., and Sorokov, D. S.: Arctic oil and gas super
30     basin, X World Petroleum Congress, London, 93-99, 1983.
31 Graversen, R. G., Mauritsen, T., Tjernstrom, M., Kallen, E., and Svensson, G.: Vertical structure
32     of recent Arctic warming, Nature, 451, 53-56, 2008.
33 Greinert, J., McGinnis, D. F., Naudts, L., Linke, P., and De Batist, M.: Atmospheric methane
34     flux from bubbling seeps: Spatially extrapolated quantification from a Black Sea shelf area,
35     Journal of Geophysical Research, 115, 2010.
36 Greinert, J. and Nützel, B.: Hydroacoustic experiments to establish a method for the
37     determination of methane bubble fluxes at cold seeps, Geo-Marine Letters, 24, 75-85, 2004.
38 Hölemann, J. A., Kirillov, S., Klagge, T., Novikhin, A., Kassens, H., and Timokhov, L.: Near-
39     bottom water warming in the Laptev Sea in response to atmospheric and sea-ice conditions in
40     2007, 2011, doi: 10.3402/polar.v30i0.6425, 2011. 2011.
41 Hornafius, S. J., Quigley, D. C., and Luyendyk, B. P.: The world's most spectacular marine
42     hydrocarbons seeps (Coal Oil Point, Santa Barbara Channel, California): Quantification of
43     emissions, Journal Geophysical Research - Oceans, 104, 20703-20711, 1999.
44 Judd, A. and Hovland, M.: Seabed fluid flow: The impact on geology, biology and the marine
45     environment, Cambridge University Press, 2007.

29

Leifer, I.: Characteristics and scaling of bubble plumes from marine hydrocarbon seepage in the Coal Oil Point seep field, Journal Geophysical Research, 115, C11014, 2010.

Leifer, I. and Boles, J.: Measurement of marine hydrocarbon seep flow through fractured rock and unconsolidated sediment, Marine and Petroleum Geology, 22, 551-568, 2005.

Leifer, I. and Culling, D.: Formation of seep bubble plumes in the Coal Oil Point seep field, Geo-Marine Letters, 30, 339-353, 2010.

Leifer, I., Jeuthe, H., Gjøsund, S. H., and Johansen, V.: Engineered and natural marine seep, bubble-driven buoyancy flows, Journal of Physical Oceanography, 39, 3071-3090, 2009.

Leifer, I., Kamerling, M., Luyendyk, B. P., and Wilson, D.: Geologic control of natural marine hydrocarbon seep emissions, Coal Oil Point seep field, California, Geo-Marine Letters, 30, 331-338, 2010.

Leifer, I., Luyendyk, B. P., Boles, J., and Clark, J. F.: Natural marine seepage blowout: Contribution to atmospheric methane, Global Biogeochemical Cycles, 20, GB3008, 2006.

Leifer, I., McClimans, T. A., Gjøsund, S. H., and Grimaldo, E.: Fluid motions associated with engineered area bubble plumes, Journal of Waterway, Port, Coastal, and Ocean Engineering, 142, 2015a.

Leifer, I. and Patro, R.: The bubble mechanism for methane transport from the shallow sea bed to the surface: A review and sensitivity study, Continental Shelf Research, 22, 2409-2428, 2002.

Leifer, I., Solomon, E., Schneider v. Deimling, J., Coffin, R., Rehder, G., and Linke, P.: The fate of bubbles in a large, intense bubble plume for stratified and unstratified water: Numerical simulations of 22/4b expedition field data, Journal of Marine and Petroleum Geology, 68B, 806-823, 2015b.

Leifer, I. and Tang, D. J.: The acoustic signature of marine seep bubbles, Journal of the Acoustical Society of America, Express Letters, 121, EL35-EL40, 2006.

Lemke, P., Ren, J., Alley, R. B., Allison, I., Carrasco, J., Flato, G., Fujii, Y., Kaser, G., Mote, P., Thomas, R. H., and Zhang, T.: Observations: Changes in Snow, Ice and Frozen Ground. In: Climate change 2007 : The physical science basis, Contribution of Working Group 1 to the Fourth Assessment Report of the Intergovernmental Panel on Climate Change, Solomon, S., Qin, D., Manning, M., Chen, Z., Marquis, M., Averyt, K. B., Tignor, M., and Miller, H. L. (Eds.), Cambridge University Press, Cambridge, UK, 2007.

MacDonald, I.: Remote sensing and sea-truth measurements of methane flux to the atmosphere (HYFLUX project), US Department of Energy, National Energy Technology Laboratory,, 164 pp., 2011.

Maksimov, A. O., Burov, B. A., Salomatin, A. S., and Chernykh, D. V.: Sounds of undersea gas leaks. In: Underwater Acoustics and Ocean Dynamics: Proceedings of the 4th Pacific Rim Underwater Acoustics Conference, Zhou, L., Xu, W., Cheng, Q., and Zhao, H. (Eds.), Springer Singapore, Singapore, 2016.

Minnaert, M.: On musical air bubbles and the sound of running water, Philosophical Magazine, 16, 235-248, 1933.

Muyakshin, S. I. and Sauter, E.: The hydroacoustic method for the quantification of the gas flux from a submersed bubble plume, Oceanology, 50, 995-1001, 2010.

Nicolsky, D. and Shakhova, N.: Modeling sub-sea permafrost in the East-Siberian Arctic Shelf: the Dmitry Laptev Strait, Environmental Research Letters, 5, 2010.

30

Nicolsky, D. J., Romanovsky, V. E., Romanovskii, N., Kholodov, A. L., Shakhova, N. E., and Semiletov, I.: Modeling sub-sea permafrost in the East Siberian Arctic Shelf: The Laptev Sea region, Journal of Geophysical Research, 117, F03028, 2012.

Osterkamp, T. E.: Subsea Permafrost. In: Climate and Oceans, John H. Steele, Steve A. Thorpe, and Turekian, K. K. (Eds.), Academic Press, London UK, 2010.

Rehder, G., Keir, R. S., Suess, E., and Rhein, M.: Methane in the Northern Atlantic controlled by microbial oxidation and atmospheric history, Geophysical Research Letters, 26, 587-590, 1999.

Rehder, G., Leifer, I., Brewer, P. G., Friederich, G., and Peltzer, E. T.: Controls on methane bubble dissolution inside and outside the hydrate stability field from open ocean field experiments and numerical modeling, Marine Chemistry, 114, 19-30, 2009.

Romanovskii, N. N., Hubberten, H.-W., Gavrilov, A. V., Eliseeva, A. A., and Tipenko, G. S.: Offshore permafrost and gas hydrate stability zone on the shelf of East Siberian Seas, Geo-Marine Letters, 25, 167-182, 2005.

Römer, M., Sahling, H., Pape, T., Bohrmann, G., and Spieß, V.: Quantification of gas bubble emissions from submarine hydrocarbon seeps at the Makran continental margin (offshore Pakistan), Journal of Geophysical Research: Oceans, 117, C10015, 2012.

Sahling, H., Bohrmann, G., Artemov, Y., G.,, Bahr, A., Brüning, M., Klapp, S., A.,, Klaucke, I., Kozlova, E., Nikolovska, A., Pape, T., Reitz, A., and Wallmann, K.: Vodyanitskii mud volcano, Sorokin trough, Black Sea: Geological characterization and quantification of gas bubble streams, Marine and Petroleum Geology, 26, 1799-1811, 2009.

Sauter, E. J., Muyakshin, S. I., Charlou, J.-L., Schlüter, M., Boetius, A., Jerosch, K., Damm, E., Foucher, J.-P., and Klages, M.: Methane discharge from a deep-sea submarine mud volcano into the upper water column by gas hydrate-coated methane bubbles, Earth and Planetary Science Letters, 243, 354-365, 2006.

Schneider von Deimling, J., Brockhoff, J., and Greinert, J.: Flare imaging with multibeam systems: Data processing for bubble detection at seeps, Geochemistry, Geophysics, Geosystems, 8, 1-7, 2007.

Schneider von Deimling, J., Greinert, J., Chapman N.R., Rabbel, W., and Linke, P.: Acoustic imaging of natural gas seepage in the North Sea: Sensing bubbles controlled by variable currents, Limnology and Oceanography Methods, 8, 155-171, 2010.

Schneider von Deimling, J., Rehder, G., Greinert, J., McGinnis, D. F., Boetius, A., and Linke, P.: Quantification of seep-related methane gas emissions at Tommeliten, North Sea, Continental Shelf Research, 31, 867-878, 2011.

Semiletov, I. P., Shakhova, N. E., Pipko, I. I., Pugach, S. P., Charkin, A. N., Dudarev, O. V., Kosmach, D. A., and Nishino, S.: Space–time dynamics of carbon and environmental parameters related to carbon dioxide emissions in the Buor-Khaya Bay and adjacent part of the Laptev Sea, Biogeosciences, 10, 5977-5996, 2013.

Semiletov, I. P., Shakhova, N. E., Sergienko, V. I., Pipko, I. I., and Dudarev, O. V.: On carbon transport and fate in the East Siberian Arctic land-shelf-atmosphere system, Environmental Research Letters, 7, 2012.

Serreze, K. C., Stroeve, J., Mauritzen, C., Cazenave, A., Rignot, E., Bates, N. R., Canadell, J. G., Raupach, M. R., Shakhova, N., and Semiletov, I.: Arctic climate feedbacks: Global implications, World Wildlife Foundation, 98 pp., 2009.

Shakhova, N. and Semiletov, I.: Methane release and coastal environment in the East Siberian Arctic Shelf, Journal of Marine Systems, 66, 227-243, 2007.

Shakhova, N., Semiletov, I., Leifer, I., Rekant, P., Salyuk, A., and Kosmach, D.: Geochemical and geophysical evidence of methane release over the East Siberian Arctic Shelf, Journal of Geophysical Research., 115, C08007, 2010a.

Shakhova, N., Semiletov, I., Salyuk, A., Iossoupov, V., Kosmach, D., and Gustafsson, O.: Extensive methane venting to the atmosphere from sediments of the East Siberian Arctic Shelf, Science, 327, 1246-1249, 2010b.

Shakhova, N., Semiletov Igor P., Leifer, I., Sergienko, V., Salyuk, A., Kosmach, D., Chernikh, D., Stubbs, C., Nicolsky, D., Tumskoy, V., Alexeev, V., and Gustafsson, O.: Ebullition and storm-induced methane release from the East Siberian Arctic Shelf, Nature Geoscience, 7, 64-70, 2014.

Shakhova, N., Semiletov Igor P., Valentin Sergienko, Leopold Lobkovsky, Yusupov, V., Salyuk, A., Salomatin, A., Chernykh, D., Kosmach, D., Panteleev, G., Joye, S., Charkin, A., Dudarev, O., Meluzov, A., and Gustafsson, O.: The East Siberian Arctic Shelf: Towards further assessment of permafrost-related methane fluxes and role of sea ice, Philosophical Transactions of the Royal Society A: Mathematical, Physical and Engineering Sciences, 373, 1-13, 2015.

Shakhova, N. E. and Semiletov, I. P.: Methane Hydrate Feedbacks, WWF International Arctic Programme978-2-88085-305-1, 81-92 pp., 2009.

Solomon, E., Kastner, M., MacDonald, I. R., and Leifer, I.: Considerable methane fluxes to the atmosphere from hydrocarbon seeps in the Gulf of Mexico, Nature Geoscience, 2, 561-565, 2009.

Soloviev, V. A., Ginzburg, G. D., Telepnev, E. V., and Mihalyuk, Y. N.: Cryothermia and natural gas hydrates within the Arctic Ocean, Sevmorgeologiya, Leningrad, 1987.

Stubbs, C.: Spatial distribution of near-shore gas seepage from sub-sea permafrost in the Laptev Sea Shelf, Arctic Ocean, MS, Geological Sciences, University of California, Santa Barbara, Santa Barbara, 118 pp., 2010.

Tsuchiya, K., Ohsaki, K., and Taguchi, K.: Large and small bubble interaction patterns in a bubble column, International Journal of Multiphase Flow, 22, 121-132, 1996.

Veloso, M., Greinert, J., Mienert, J., and De Batist, M.: A new methodology for quantifying bubble flow rates in deep water using splitbeam echosounders: Examples from the Arctic offshore NW-Svalbard, Limnology and Oceanography: Methods, doi: 10.1002/lom3.10024, 2015. n/a-n/a, 2015.

Warzinski, R. P., Lynn, R., Hasljasmaa, I., Leifer, I., Shaffer, F., Anderson, B. J., and Levine, J. S.: Dynamic morphology of gas hydrate on a methane bubble in water: Observations and new insights for hydrate film models, Geophysical Research Letters, 41, 6841-6847, 2014.

Weber, S. A., Engel-Cox, J. A., Hoff, R. M., Prados, A. I., and Zhang, H.: An improved method for estimating surface fine particle concentrations using seasonally adjusted satellite aerosol optical depth, Journal of the Air & Waste Management Association, 60, 574-585, 2010.

Weber, T. C.: Observations of clustering inside oceanic bubble clouds and the effect on short-range acoustic propagation, Journal of the Acoustical Society of America, 124, 2008.

Weber, T. C., Mayer, L., Jerram, K., Beaudoin, J., Rzhanov, Y., and Lovalvo, D.: Acoustic estimates of methane gas flux from the seabed in a 6000 km2 region in the Northern Gulf of Mexico, Geochemistry, Geophysics, Geosystems, 15, 1911-1925, 2014.

Wilson, D., Leifer, I., and Maillard, E.: Megaplume bubble process visualization by 3D multibeam sonar mapping, Journal of Marine and Petroleum Geology, 68, 753-765, 2015.